

The genesis of phosphatic and carbonate rocks in the Toyoma Formation, Northeastern Japan

Toshiro MORIKIYO*, Kinuko MATSUNAGA*, Kazuo IWAMASA*
Satoshi KANISAWA** and Yuichi MORISHITA***

**Department of Geology, Faculty of Science, Shinshu University, Asahi 3-1-1,
Matsumoto 390-8621, Japan*

***2-19-14, Yagiyama-Honcho, Taihaku-ku, Sendai 982-0801, Japan*

****Geological Survey of Japan, AIST, Central 7, Higashi 1-1-1, Tsukuba 305-8567, Japan*

(Received March 2, 2011)

Contents

Abstract

- I Introduction
- II Geologic outline and petrography
- III Calculation of rock norms
- IV Analytical methods
 1. Sulfur isotopes
 2. Secondary ion mass spectrometry
 3. Carbon and oxygen isotopes
 4. Trace elements
- V Results
 1. Carbon and oxygen isotopes
 2. Sulfur isotopes
 3. Pyrite types
 4. Sulfur isotope microanalysis
 5. Rock norms
- VI Discussion
 1. Cause of $\delta^{34}\text{S}$ variation in pyrite
 2. Phosphatic nodules
 - (1) Source of phosphorus
 - (2) The site of phosphatic nodule formation
 - (3) The period of phosphatic nodule formation
 - (4) The cause of apatite precipitation
 3. Diagenetic zones
 - (1) Zone 3
 - (2) Zone 2

- (3) Zone 1
 - 4. Early diagenesis of the Toyoma Formation
 - (1) Zone 1
 - (2) Zone 2
 - (3) Zone 3
 - 5. Formative process of each rock type
 - (1) Phosphatic nodules
 - (2) A-type rock
 - (3) B-type rock
 - (4) C-type rock
 - (5) Black shale
 - 6. Diagenetic segregation
- VII Conclusions
- Acknowledgements
- References
- Appendix
- Plates and explanations

Abstract

Various phosphatic and carbonate rocks occur in the Upper Permian Toyoma Formation. They are classified into phosphatic nodules, A-, B- and C-type rocks. The isotopic ratios of whole-rock calcite, pyrite and apatite in the rocks and the results of pyrite microanalysis using a high-resolution secondary ion mass spectrometer are presented. The carbon and sulfur isotopic compositions indicate that the rocks were formed through microbial sulfate reduction.

Three distinct zones have been recognized within the Toyoma Formation that define its early diagenesis. The three zones' compositions differ in their mole fractions of authigenic material and the $\delta^{13}\text{C}$ of their calcite deposits. Zone 1 is the region of oxic surface sediment in which sulfur-oxidizing bacteria grew. Because sulfuric acid is generated by the chemosynthesis of the bacteria, biogenic phosphate debris such as fish bones and scales were dissolved. The phosphate ions thus formed were the source of the phosphatic rocks of the Toyoma Formation. Zone 2 is the anoxic zone that underlay Zone 1. Anaerobic sulfate-reducing bacteria grew in this zone, resulting in increased pore water alkalinity and the precipitation of pyrite and apatite. Phosphatic nodules and A- and B-type rocks began to grow in this zone. Zone 3 is characterized by calcite precipitation. The pore water, saturated with

calcite components, segregated from the sediments into rocks allowing the rocks to be calcareous. As sediments became buried deeper and deeper, they experienced the conditions of each successive zone. However, the period of final consolidation of the rocks differed from one rock type to another as evidenced by the varying $\delta^{13}\text{C}$ values for calcite contained in the different rock types. Although the rocks are mixtures of authigenic minerals originating in different zones, it was possible to estimate the range of diagenetic zones in which each rock type was formed.

I Introduction

The occurrence of various phosphatic and carbonate rocks in the Upper Permian Toyoma Formation was first reported by Kanisawa and Ehiro (1986). They divided the rocks into four types on the basis of their modes of occurrence and lithology: 1) phosphatic nodules, 2) A-type rock (phosphate-bearing calcareous shale), 3) B-type rock (coarse, gray-colored, calcareous sandstone), and 4) C-type rock (massive, grayish, sparitic limestone). Phosphate is dominant in the phosphatic nodules and A-type rock, while carbonate is dominant in B- and C-type rocks. They reported the whole-rock chemical compositions of the rocks and described their chemical characteristics.

Morikiyo et al. (1994) reported on the carbon and oxygen isotope compositions of calcite contained in the rocks. The $\delta^{13}\text{C}$ values of the rocks were found to be very low, ranging from -15.8 to -6.8‰ . They concluded that the rocks were formed by microbial sulfate reduction. Morikiyo and Matsunaga (2001) reported isotopic ratios of pyrite and apatite in these rocks and confirmed the view of Morikiyo et al. However, the question of why apatite precipitates in the early stage of diagenesis has not been definitively resolved.

In this paper, the genesis of the phosphatic and carbonate rocks in the Toyoma Formation is explained, based mainly on answers to two critical problems; 1) the source of phosphorus in the rocks and 2) the depth of sediment burial in which authigenic apatite precipitated. Then the formative process of the four rock types (i. e., phosphatic nodules, A-, B- and C-type rocks) is discussed in detail and an entire picture of the early diagenesis of the Toyoma Formation is described.

II Geologic outline and petrography

The Upper Permian Toyoma Formation is composed mainly of black-colored, fine-grained, homogeneous shale and contains a thin, intercalated sandstone bed. The shale shows strong slaty cleavage. The total thickness of the formation is deduced to be 1500-2000 m. Since the occurrence of fossils in the formation is rare and the shale has a characteristic black appearance, it has been thought that it was deposited in an enclosed inland sea in an anaerobic environment (Minato, 1950). Ammonites have been

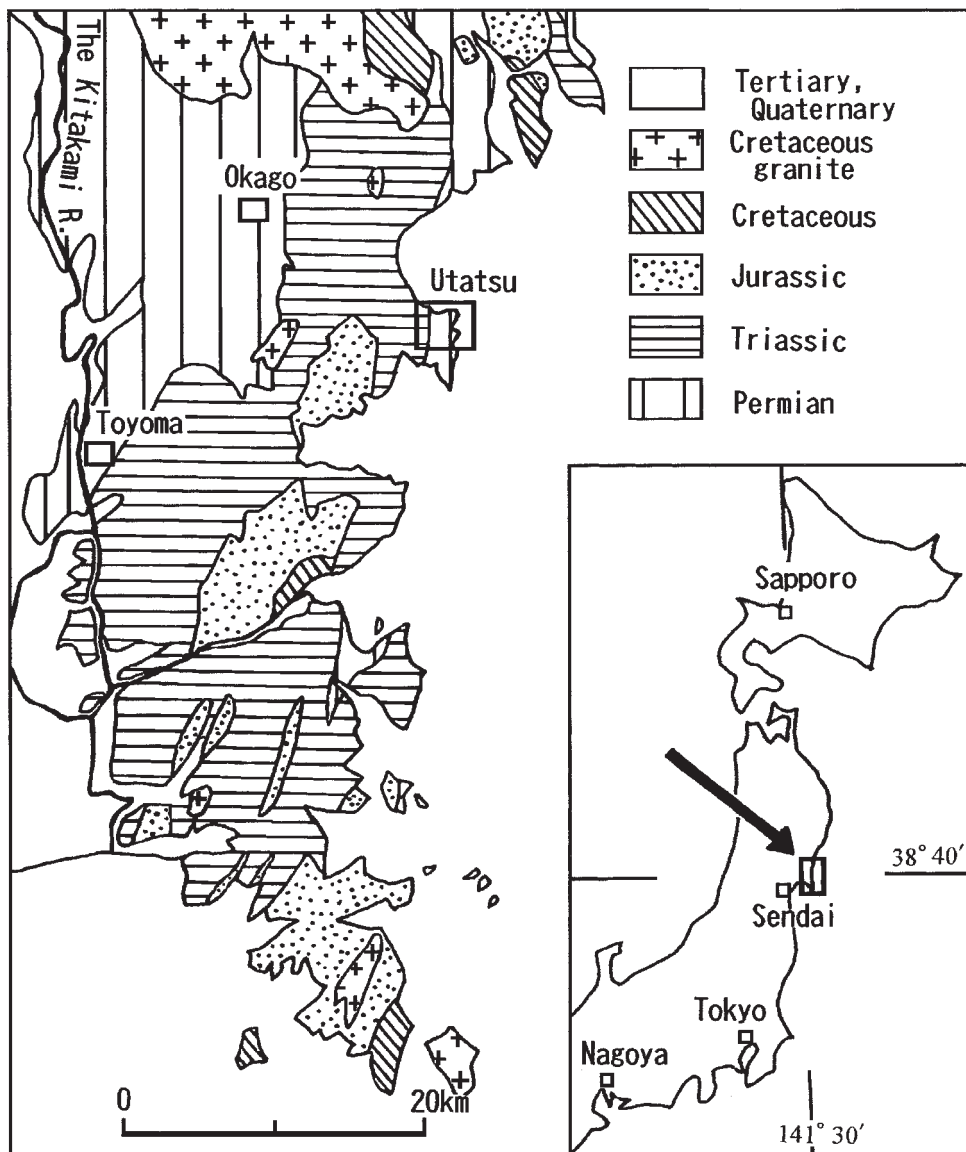


Fig. 1. Map showing the distribution of Paleozoic and Mesozoic strata in the South Kitakami Belt and the locations of study areas. Most samples were collected from the Utatsu area.

found recently, leading to the belief that the Toyoma Formation developed during the Dzhulfian (Wujapingian) and Dorashamian (Chagxingian) ages (Ehiro and Bando, 1985). According to Kamada (1998), Toyoma Formation sediments were deposited in environments such as a muddy shelves, channel-slopes, or the slopes to basin floors.

Phosphatic and carbonate rocks occur in the Utatsu, Okago and Toyoma areas (Fig. 1). In this paper, rocks with a P_2O_5 content one or two orders of magnitude greater than normal sediments are called phosphatic following the definition by Pettijohn (1975). Most of the phosphatic and carbonate rock samples were taken from the coast in the Utatsu area, where the Toyoma Formation, reaching about 1400 m in thickness, has been subdivided into the Suenosaki and Tanoura formations (in ascending order). Ehiro and Bando (1985) and Kamada (1993) have detailed the geology of this area.

The phosphatic rocks as well as the black shale contain pyrite of various types. The pyrite was classified morphologically into the following four types by Endo et al. (1973): (a) framboidal pyrite: spherical aggregates of micro-sized crystals (Plate II-1, -2, IV-1, -2, -3), (b) minute pyrite: crystals less than $1 \mu\text{m}$ scattered in a rock matrix (Plate IV-3, -4), (c) large, euhedral pyrite: larger cubes from 10 to $100 \mu\text{m}$ in diameter (Plate IV-6), and (d) irregular-shaped pyrite: irregularly shaped aggregates. We follow the same classification and measured the occurrences of each pyrite type by using a point counter under a reflection microscope. The proportions of each pyrite type in various samples are shown in Table 2.

Black shale: Black shale is black-colored, fine-grained siltstone or mudstone with slaty cleavages. It is composed of quartz, albite, chlorite, illite-muscovite, pyrite and carbonaceous matter. Although the shale is black in appearance, the amount of carbonaceous matter contained is not high judging from its chemical analysis. Two pyrite types occur: framboidal (30-65%), and minute crystals (35-70%). Framboidal pyrite is commonly seen under the microscope (Plate II-1, -2) and aggregates of up to 5 mm in diameter of pyrite crystals are sometimes found. Carbonate minerals were not found in the samples studied.

The phosphatic nodules reported in Kanisawa and Ehiro (1986) are classified into the following two subtypes in this paper: (a) phosphatic nodules without a pyritiferous core (Plate I -1, -2), and (b) phosphatic nodules with a pyritiferous core (Plate I -3). Hereafter nodules of subtype (a) are referred to as phosphatic nodules for convenience.

Phosphatic nodules: These occur in the black shale as black-colored, ellipsoidal concretions having a diameter of several centimeters. They are embedded in phosphate-bearing mudstone or phosphate-bearing calcareous mudstone. In seaside outcrops, the rims of the phosphatic nodules have sometimes been dissolved (Plate I -2). This indicates that the nodules have a carbonate rim. Under the microscope, the nodule consists mainly of pale brownish, cryptocrystalline apatite with small amounts of detrital quartz and albite grains. Spheluritic fossil-like objects replaced by calcite are

occasionally seen (Plate II-3, -4). The types of pyrite present are : framboidal (0- 5%), minute crystals (45-100%), euhedral (0-35%), and irregular-shaped pyrites (0-10%). Phosphatic nodules are not common throughout all of the Toyoma Formation. In some localities, several phosphatic nodules tend to be found clustered in a certain horizon, suggesting that their occurrence was controlled by the chemistry of the host sediments.

Phosphatic nodules with a pyritiferous core : In some phosphatic nodules, coarse-grained, euhedral crystals of pyrite cluster at the center of the nodules (Fig. 8, Plate I -3). However, the mantle lithology of these nodules is the same that of phosphatic nodules without a pyritiferous core. Pyrite types occurring in the central part of the nodules are : framboidal (0-2%), minute crystal (15-40%), and euhedral crystal (60-80%). The pyrite type in the core of the nodules is characteristically large and euhedral.

A-type : A-type rock is grayish black-colored, fine-grained, homogeneous mud or siltstone free from slaty cleavage. It occurs as thin beds 2 to 5 cm thick (Fig. 2-1) or in thin lenses in the black shale. A-type rock is invariably accompanied by C-type rock. A sandwich structure with alternating beds of C- and A-types is frequently observed (Fig. 2-2, -4, Plate I -4). A-type rock is also interbedded with B-type rock (Fig. 2-1). In these cases, the boundary between the different rock types, or the boundary between these beds and surrounding black shale, is usually sharp. The total thickness of one set of interbedded A-, B- and C-types is generally less than 20 cm. The lithologic character of A-type rock is similar to that of phosphatic nodules except that the A-type rock contains much more calcite. Under the microscope, this rock type is composed of brownish cryptocrystalline apatite and yellow-brownish, fine-grained calcite filling the interstices between fine-grained detrital crystals (Plate II-3, -4). Pyrite types in A-type rock are : framboidal (25-45%), minute crystals (25-70%), and euhedral crystals (0-20%).

B-type : B-type rock is coarse-grained, gray calcareous sandstone (Fig. 2-3). Fragments of rocks and detrital crystals are cemented with brownish-colored calcite and fine-grained matrix materials (Plate III-3, -4). The calcite crystals are zoned optically : the cores of the calcite crystals are brownish in color while the margins are colorless and transparent (Plate II-6). Pyrite types occurring in B-type rock are : framboidal (0-35%), minute crystals (10-70%), and euhedral crystals (7-70%). B-type rock is characterized by the dominance of large, euhedral pyrite (Endo et al., 1973). The total pyrite content in these rocks, however, varies from sample to sample.

C-type : This type is a massive, grayish carbonate rock, occurring in the black shale either as thin beds several centimeters thick (Fig. 2-1, -2, -3, -4), or veins intruding into the black shale (Fig. 2-5). Thin C-type beds are usually interbedded with A- and B-type rocks (Fig. 2-1), whereas C-type veins tend to appear alone. An abundance of rectangular fragments of black shale several centimeters in size are

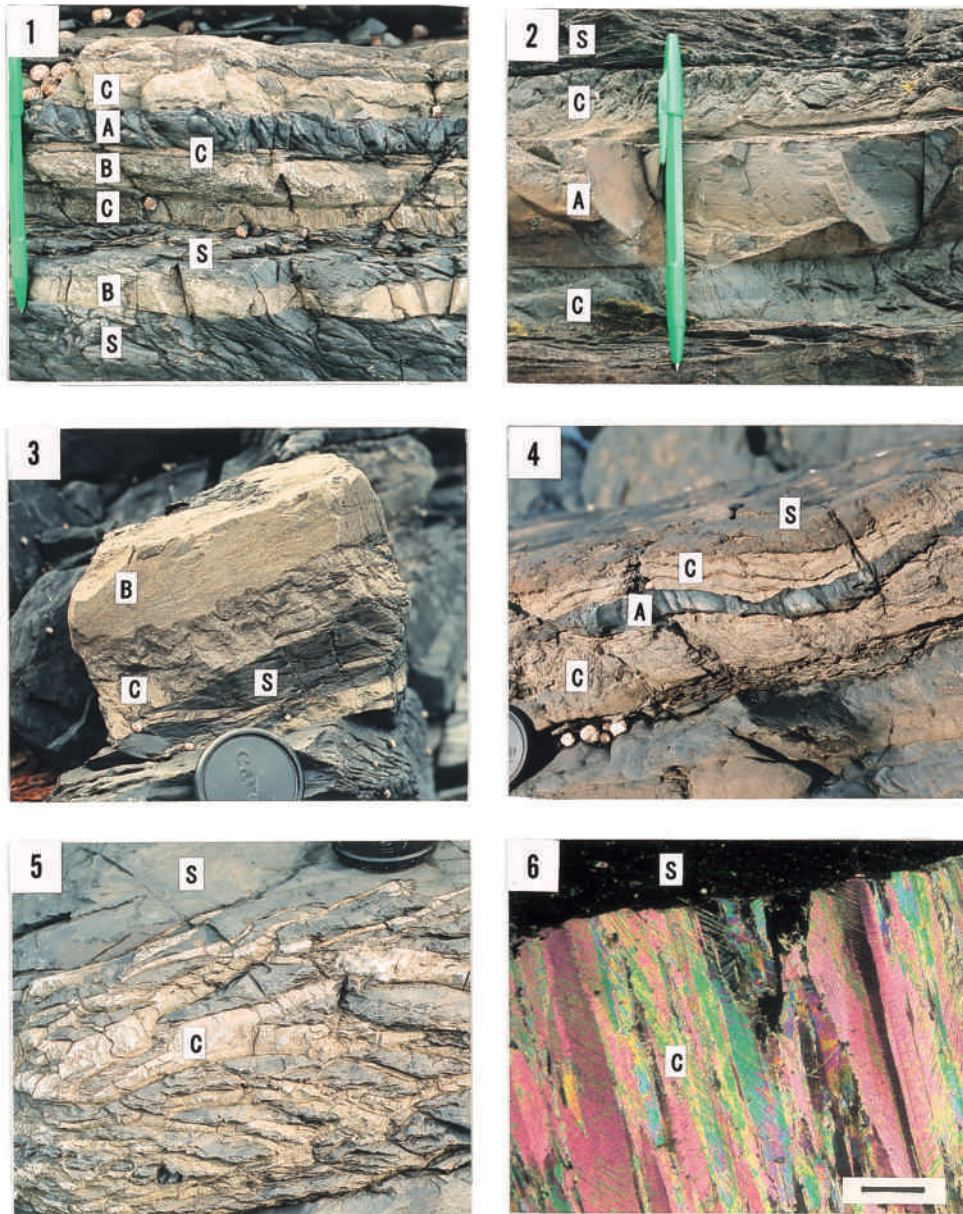


Fig. 2. Occurrences of phosphatic and carbonate rocks in the Utatsu area (1)–(5), and a photomicrograph of C-type rock (6). (1) Interbedded A-, B-, and C-type rocks. (2) A-type rock sandwiched between C-type layers. Samples taken from this exposure are KI02-3a (A-type rock, $\delta^{13}\text{C} = -11.5\%$), and KI02-3c (C-type rock, $\delta^{13}\text{C} = -12.4\%$). (3) B-type rock associated with C-type rock. Samples taken from this exposure are KI01-3a (B-type rock, $\delta^{13}\text{C} = -13.2\%$), and KI01-3b (C-type rock, $\delta^{13}\text{C} = -15.1\%$). (4) A-type rock layer enclosed in C-type rock layers. (5) Veins of C-type rock intruding into the black shale. (6) Bladed crystals of calcite in C-type rock. Crossed nicols. Scale bar = 1 mm. Abbreviations are: A: A-type rock; B: B-type rock; C: C-type rock; S: Black shale.

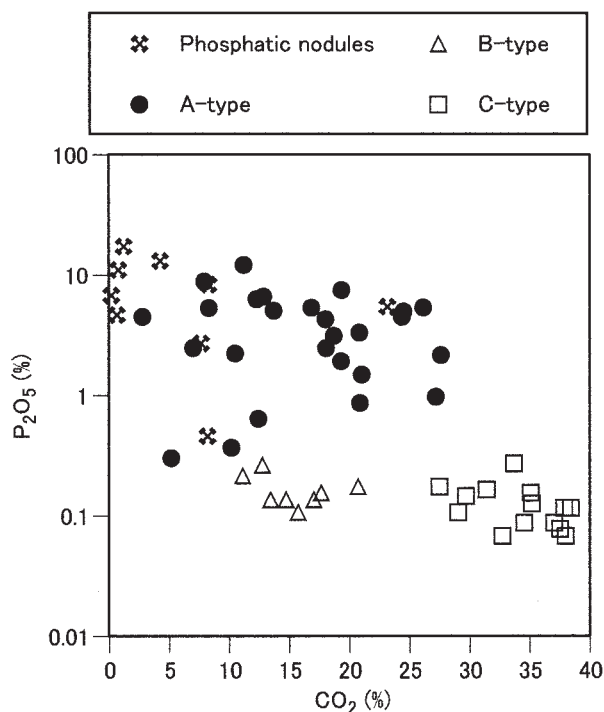


Fig. 3. Plot of whole-rock P_2O_5 content (by weight percent) against CO_2 content for phosphatic and carbonate rocks in the Toyoma Formation. The P_2O_5 content is plotted on a logarithmic scale.

enclosed in the thick portion of lenticular C-type beds (Plate I -5). Thin, wavy films of black shale are commonly enclosed in C-type rock (Fig. 2-3, Plate I -6, III-5, -6). The weathered surface of C-type rock shows streaks lined up perpendicular to the bedding plane (Fig. 2-1, -5). This is due to the parallel arrangement of large, bladed crystals of calcite in the rock (Fig. 2-6, Plate III-6, and Fig. 3B of Kanisawa and Ehiro, 1986). C-type rock was previously identified as an impure marine limestone, but it is now clear that they are carbonate veins of diagenetic origin. The field occurrence of C-type rock was detailed in Morikiyo et al. (1994).

Kanisawa and Ehiro (1986) reported the concentrations of major elements in the phosphatic and carbonate rocks. According to their results, there is a negative correlation between P_2O_5 and CO_2 contents, as shown in Fig. 3. The whole-rock CO_2 content increases in the following order: phosphatic nodules, A-, and C-type rocks. The carbonate mineral contained in the rocks is calcite, while other carbonate minerals such as dolomite, ankerite and siderite are absent. Calcite in the phosphatic and carbonate rocks in the Toyoma Formation is characterized by a high manganese oxide (MnO) content (Kanisawa and Ehiro, 1986).

III Calculation of rock norms

It is widely accepted that nodules in sedimentary rocks are formed through the precipitation of authigenic minerals during diagenesis. As was discussed in Morikiyo et al. (1994), not only phosphatic nodules but also A-, B- and C-type rocks were formed through the precipitation of authigenic minerals. Thus, the whole-rock chemical compositions of these rocks must have two different components, one of which is initial clastic material while the other is made up of authigenic minerals precipitated after deposition of the sediments. In order to estimate the composition of materials added during diagenesis, the amount and proportions of authigenic minerals contained in a rock sample were calculated from the whole-rock chemical compositions in a manner similar to CIPW norm calculations. For the calculations, the major element concentrations for both phosphatic and carbonate rocks reported by Kanisawa and Ehiro (1986) were used. The normative minerals adopted here are pyrite (FeS_2), fluorapatite ($\text{Ca}_5(\text{PO}_4)_3\text{F}$), calcite ($\text{Ca}_{0.94}\text{Mg}_{0.02}\text{Fe}_{0.01}\text{Mn}_{0.03}\text{CO}_3$), and the "mineral" of which the black shale is composed (averaged composition of JSL-1 and JSL-2; Terashima et al., 1990). The composition of calcite was estimated from the analyses of acid-soluble components in the rocks (Kanisawa and Ehiro, 1986). The black shale component cannot be accepted as a normative mineral for calculations having to do with B-type rock, because the B-type rocks are sandstone. Thus the composition of average graywacke (Pettijohn, 1975) was used. The details of the calculations are described in the Appendix. X values such as X_{Shale} , X_{Pyrite} , represent the mole fractions of the normative mineral. For those samples on which complete chemical analyses were conducted, the sums of the X values are close to 1.0 (Table 4-1), indicating that the rocks are predominantly composed of the four normative minerals adopted here.

IV Analytical methods

1. Sulfur isotopes

The ground phosphatic rock samples were thoroughly washed with distilled water to remove soluble sulfates, although water-soluble sulfates such as gypsum were not, in fact, detected. The washed powder samples were then treated with 6N HCl for 24 hours to extract sulfate within the apatite lattice. The sulfate ions were subsequently precipitated as BaSO_4 . The residue after the acid treatment of the rocks contains pyrite, from which sulfur was then extracted.

Pyrite in the black shale and phosphatic rocks was decomposed with hydrochloric (HCl)+nitric(HNO_3) acids (mixing ratio of 1 : 3). The potential effect of SO_4^{2-} contamination from organic matter is likely negligible because the sulfur concentration was very low. The BaSO_4 thus obtained was heated with V_2O_5 and SiO_2 up to 950 °C and

converted to SO₂ gas, following the procedure described by Yanagisawa and Sakai (1983). Sulfur isotopic measurements were made with a Delta E mass spectrometer in the Geological Institute of the University of Tokyo. The measured isotopic ratios were corrected by using the equation given in Shimazaki (1985). The isotopic ratios of the sulfur are reported in terms of the δ notation relative to CDT. The total analytical uncertainty in $\delta^{34}\text{S}$ values is estimated to be $\pm 0.2\%$.

2. Secondary ion mass spectrometry

Sulfur isotope ratio measurements for the individual pyrite grains in sample KI01-4 were carried out using a Cameca ims-1270 SIMS at the Geological Survey of Japan, AIST. A defocused Cs⁺ primary beam was restricted to 12 μm in diameter by a circular aperture to obtain a homogeneous primary beam of about 0.4 nA. Negative secondary ions of sulfur were uniformly sputtered by the primary beam with total impact energy of 20 kV. A normal-incidence electron gun was used for charge compensation on the sample.

The secondary ³²S and ³⁴S ions were simultaneously detected using two Faraday cups of the multicollection system of the SIMS. An energy window of 50 eV was adjusted to the energy distribution curve to make sure that we always collect the same energy band of S⁻ ions. The precision of $\delta^{34}\text{S}$ value (2δ error) is less than 0.2%. Analytical techniques other than described here were based on Morishita et al. (1997).

Description of analyzed sample (KI01-4): KI01-4 is a carbonate-rich phosphatic nodule collected from the Suenosaki Formation at the seaside of Utatsu. It is ellipsoidal, 10 cm long and is without a pyritiferous core. Whole-rock P₂O₅ and CO₂ content is 2.06 and 26.97%, respectively. The complete chemical analysis was not made. Authigenic minerals are pyrite of various morphology, calcite and apatite. Whole-rock pyrite $\delta^{34}\text{S}$ is -21.0% , and the proportion of pyrite types present are: framboidal (6%), minute (42%), euhedral (35%), and irregular shaped pyrite (16%). $\delta^{13}\text{C}$ of calcite is -9.5% . The pyrite grains chosen for microanalysis are presented in Table 3 and shown in Fig. 10.

3. Carbon and oxygen isotopes

All the carbonate in the phosphatic and carbonate rocks was identified as calcite by X-ray diffraction analysis. The procedure for extracting CO₂ from calcite followed that outlined by McCrea (1950). The isotopic compositions of the CO₂ were measured by the use of a MAT250 mass spectrometer at Shinshu University. The oxygen isotope fractionation factor determined by Sharma and Clayton (1965), $\alpha_{\text{CO}_2\text{-CC}}=1.01025$, was used to calculate the ¹⁸O/¹⁶O ratio of the calcite. The isotopic data are presented in terms of δ notation relative to PDB for carbon and SMOW for oxygen. The analytical uncertainty is about $\pm 0.1\%$ for both $\delta^{13}\text{C}$ and $\delta^{18}\text{O}$ values.

X-ray diffraction analysis of apatite in the phosphatic rocks indicates that the

mineral is carbonate–fluorapatite with a CO₂ content of 0.5 to 4.0% by weight (Morikiyo et al., 2004). The CO₂ concentration of the apatite was estimated using the equation given in Gulbrandsen (1970). Thus, the CO₂ extracted from phosphatic rocks during carbon and oxygen isotopic analysis may be slightly contaminated with CO₂ from the apatite. However, we infer that there is no effect of this on the $\delta^{13}\text{C}$ and $\delta^{18}\text{O}$ values of calcite, because the CO₂ concentration of apatite, as well as the amount of apatite present in the rock samples, are exceedingly small.

4. Trace elements

The whole-rock concentrations of trace elements including rare earth elements were analyzed using inductively coupled plasma mass spectrometry (ICP-MS) at ALS Chemex, Canada.

V Results

1. Carbon and oxygen isotopes

The carbon and oxygen isotopic compositions of calcite contained in phosphatic and carbonate rocks of the Toyoma Formation have been reported by Morikiyo et al. (1994). Additional analyses were made in the present study. They are shown together with values reported in Morikiyo et al. (1994) in Table 1 and illustrated in Fig. 4 and Fig. 5. Since calcite does not occur in the black shale, isotopic data were not obtained.

Phosphatic nodules : The $\delta^{13}\text{C}$ values for the phosphatic nodules range from -10.5 to -6.8‰ . The $\delta^{18}\text{O}$ values for the nodules fall in a range between 15.2 and 17.9‰. Since calcite is lacking in the typical (i.e. high P₂O₅ content) phosphatic nodule, carbon and oxygen isotopic data could not be obtained.

Phosphatic nodules with pyritiferous cores : The carbon and oxygen isotopic analysis for this nodule subtype was done only for sample U-N011. Although calcite occurs only in the marginal part of the nodule, a whole-rock sample was used for the analysis. It had a $\delta^{13}\text{C}$ of -6.9‰ and a $\delta^{18}\text{O}$ of 15.9‰. The isotopic compositions are similar to those of pyritiferous core-free phosphatic nodules.

A-type : The calcite of A-type rock has isotopic compositions ranging from -11.7 to -5.7‰ for carbon and from 14.2 to 20.7‰ for oxygen. The A-type rock (KI02-3a) sandwiched between C-type layers, shown in Fig. 2-2, has a $\delta^{13}\text{C}$ of -11.5‰ . The C-type layer (KI02-3c) in contact with KI02-3a has a carbon isotopic composition of -12.4‰ .

B-type : The $\delta^{13}\text{C}$ for B-type rock ranges from -13.2 to -8.0‰ and the $\delta^{18}\text{O}$ ranges from 13.9 to 16.6‰. B-type rock as a whole has lower values of $\delta^{13}\text{C}$ than A-type rock (Figs. 4 and 5). The B-type rock shown in Fig. 2-3 (KI01-3a) has a $\delta^{13}\text{C}$ of -13.2‰ . The $\delta^{13}\text{C}$ of the C-type rock (KI01-3b) adjacent to KI01-3a is -15.1‰ .

Table 1 Carbon and oxygen isotopic ratio of the calcite, and chemical composition of the acid-soluble fraction of phosphatic and carbonate rocks in the Toyoma Formation.

Sample No.	P ₂ O ₅ (%)	CO ₂ (%)	δ ¹³ C (‰)	δ ¹⁸ O (‰)	FeO (%)	MnO (%)	MgO (%)	CaO (%)	Locality	δ ³⁴ S of pyrite
Phosphatic nodules										
P-20*	0.47	8.13	-6.8	17.2	0.20	0.31	0.08	9.73	U	
UP-29(3)*	13.42	4.18	-7.2	16.6	0.05	0.14	0.18	4.52	U	
O-N112'			-7.5	17.9					O	
UP-29(1)*	8.52	8.22	-7.9	17.1	0.23	0.38	0.17	9.93	U	
KI01-4*	2.06	26.97	-9.5	16.1	0.52	2.23	0.20	12.92	U	measured
KI01-2*	5.59	23.11	-10.5	15.2	0.56	2.37	0.22	14.04	U	measured
UP-59A	17.73	1.15			0.07	0.11	0.25	1.82	U	
UP-59C	11.27	0.69			0.07	0.10	0.23	1.63	U	
OP-1	4.78	0.59			0.01	0.00	0.15	0.40	O	
UP-17	6.93	0.12			0.01	0.00	0.12	0.42	U	
Phosphatic nodules with pyritiferous core										
U-N011bulk	2.77	7.60	-6.9	15.9	1.95	0.40	0.20	5.49	U	measured
A-type rock										
U-A03	5.47	8.25	-5.7	16.0	0.14	0.17	0.22	11.08	U	measured
UP-32*	4.64	2.72	-7.1	20.7	0.12	0.20	0.22	1.42	U	
U-A01	0.31	5.12	-8.9	18.4	0.63	0.17	0.28	8.81	U	measured
OP-4*	5.50	16.80	-9.0	16.1					O	
OP-6*	6.83	12.78	-9.2	16.4	0.23	0.51	0.18	15.22	O	
UP-4*	3.43	20.79	-9.9	15.1	0.26	0.69	0.22	24.34	U	
UP-11*	5.54	26.10	-10.5	14.8	0.39	0.78	0.13	30.40	U	
UP-43*	7.73	19.29	-10.5	14.2	0.10	0.44	0.16	18.61	U	
U-A11	2.3	10.43	-10.8	15.1	0.29	0.35	0.13	5.84	U	measured
OP-3*	12.51	11.15	-11.4	16.4	0.12	0.68	0.08	13.06	O	
KI02-3a*	4.41	17.97	-11.5	15.8	0.25	0.30	0.12	10.02	U	measured
U-A07			-11.7	15.4	0.26	0.01	0.17	1.21	U	measured
B-type rock										
T-B12			-8.0	15.5					T	
U-B01			-9.0	13.9	0.67	0.46	0.30	13.07	U	measured
UP-48*	0.14	13.35	-9.5	14.6	0.15	0.38	0.15	16.81	U	
U-SS10			-10.0	15.6	1.27	0.41	0.58	8.82	U	measured
UP-45*	0.14	14.64	-10.2	14.3	0.05	0.24	0.08	18.75	U	
UP-42U*	0.27	12.66	-10.5	15.1	0.09	0.30	0.10	15.51	U	
UP-4*	0.22	11.02	-10.5	15.4	0.18	0.33	0.12	12.07	U	
U-SS04			-11.2	14.8	0.19	0.26	0.06	12.77	U	measured
U-B04			-11.3	16.6	0.42	0.57	0.12	20.10	U	measured
UP-7*	0.18	20.64	-11.5	16.3	0.23	0.79	0.08	25.91	U	
U-SS14			-12.1	14.2	0.54	0.25	0.17	12.41	U	measured
U-B07			-12.3	13.9	0.96	0.30	0.34	18.80	U	measured
KI02-3b*	0.14	16.95	-12.7	15.2					U	
KI01-3a*	0.11	15.64	-13.2	14.8					U	
U-B09					0.80	0.23	0.34	5.54	U	
C-type rock										
U-C10			-11.1	14.0	0.46	0.94	0.07	38.11	U	
UP-56*	0.08	37.46	-11.4	15.2	0.48	1.37	0.21	43.08	U	
UP-50*	0.12	37.79	-11.6	15.3	0.38	1.31	0.17	45.61	U	
UP-7*	0.07	32.66	-12.0	18.1	0.36	1.34	0.15	39.42	U	
U-C08			-12.0	14.6	0.51	1.17	0.24	38.08	U	
UP-59(1)*	0.09	36.95	-12.1	15.6	0.41	1.52	0.18	43.55	U	
U-C02			-12.2	14.6	0.82	0.69	0.39	35.15	U	
KI02-3c*	0.11	18.99	-12.4	15.3					U	
KI02-2*	0.16	35.02	-12.6	18.7					U	
UP-4*	0.13	35.10	-12.8	15.3	0.55	0.74	0.23	37.11	U	
T-C21			-13.0	15.2					T	
UP-10*	0.18	27.41	-13.7	14.9	0.38	0.98	0.20	30.41	U	
U-C11			-13.9	15.7	0.57	1.14	0.20	42.44	U	measured
KI01-1*	0.28	33.62	-13.9	15.2					U	
UP-63*	0.12	38.35	-14.7	15.0	0.55	1.03	0.22	40.47	U	
UP-35*	0.15	29.63	-15.0	16.7	0.65	0.63	0.23	33.68	U	
KI01-3b*	0.09	34.48	-15.1	15.4					U	
KI02-1*	0.17	31.35	-15.8	15.2					U	

*Reproduced from Morikiyo et al. (1994). The isotopic data are presented versus PDB for carbon and SMOW for oxygen in δ notation (‰). FeO, MnO, MgO and CaO concentrations were those of acid-soluble (0.1 N acetic acid) fractions. Abbreviations for localities: U: Utatsu area; O: Okago area; T: Toyoma area.

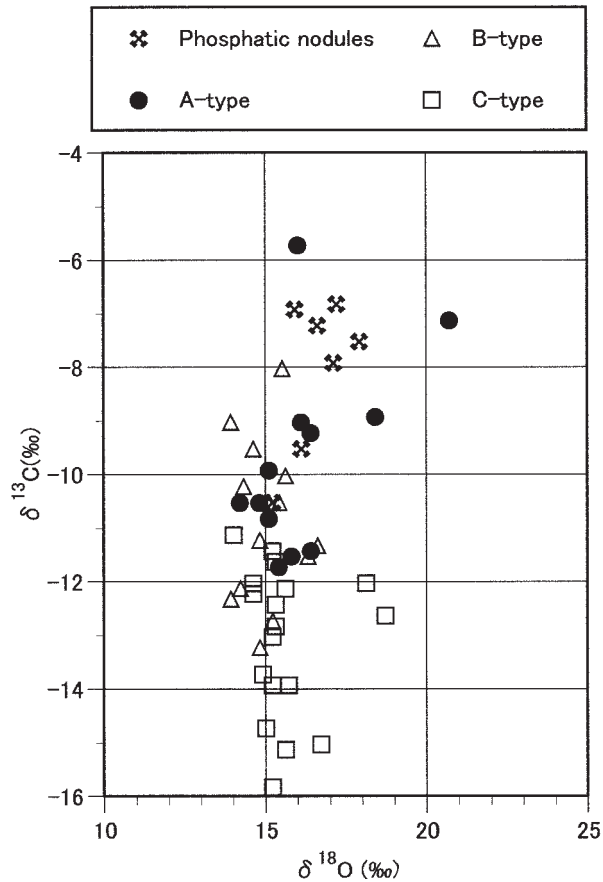


Fig. 4. Carbon and oxygen isotopic compositions of diagenetic calcite from the Toyoma Formation. $\delta^{13}\text{C}$ values are presented on the PDB scale, and $\delta^{18}\text{O}$ on the SMOW scale.

C-type: C-type rocks have a $\delta^{13}\text{C}$ ranging from -15.8 to -11.1‰ and a $\delta^{18}\text{O}$ ranging from 14.0 to 18.7‰ . The C-type carbonate rock shows the lowest carbon isotopic compositions among all the rock types in the Toyoma Formation. The $\delta^{18}\text{O}$ for the C-type rock falls in a narrow range from 14.0 to 18.7‰ with an average value of 15.6‰ .

The $\delta^{13}\text{C}$ values for these rocks are remarkably low compared with those from marine limestone (approximately -2 to $+2\text{‰}$). It is clear from Fig. 5 that $\delta^{13}\text{C}$ decreases in the following order in the rocks: phosphatic nodules, A-, B-, then C-type rocks, with some overlap. The order is the same as that for decreasing phosphorous content.

The relationship between the $\delta^{13}\text{C}$ values and CO_2 content for the rocks is shown in Fig. 6. In this figure, it can be seen that CO_2 content increases with decreasing $\delta^{13}\text{C}$,

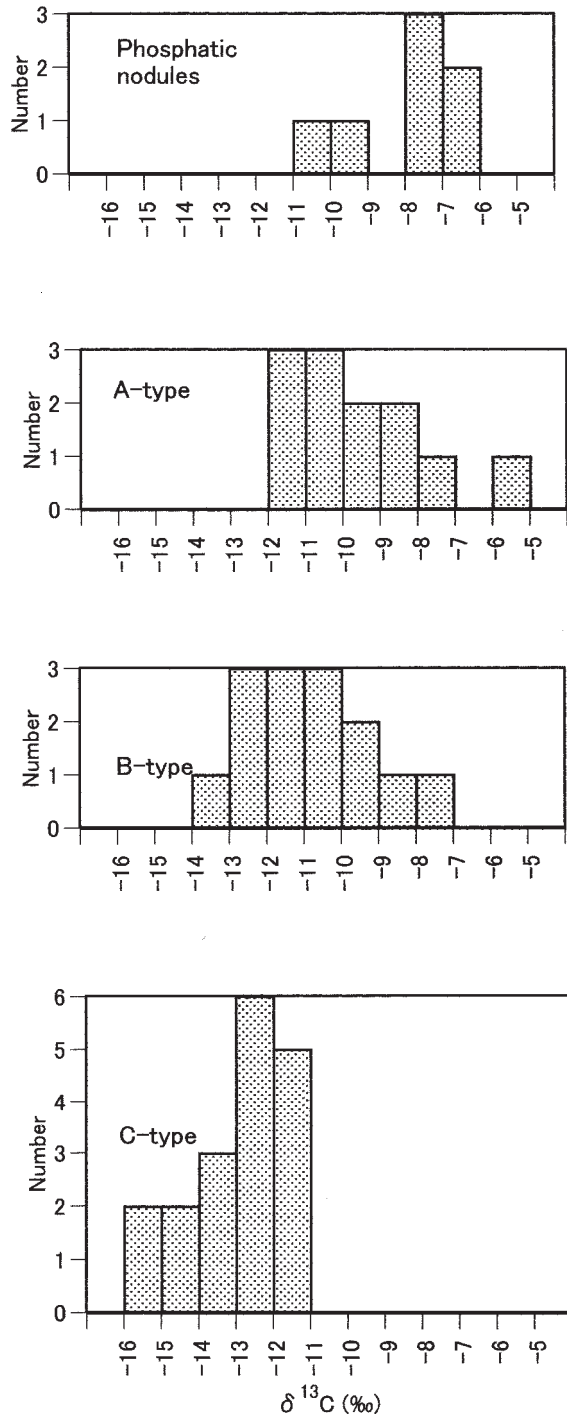


Fig. 5. Histograms showing $\delta^{13}\text{C}$ ranges for each rock type.

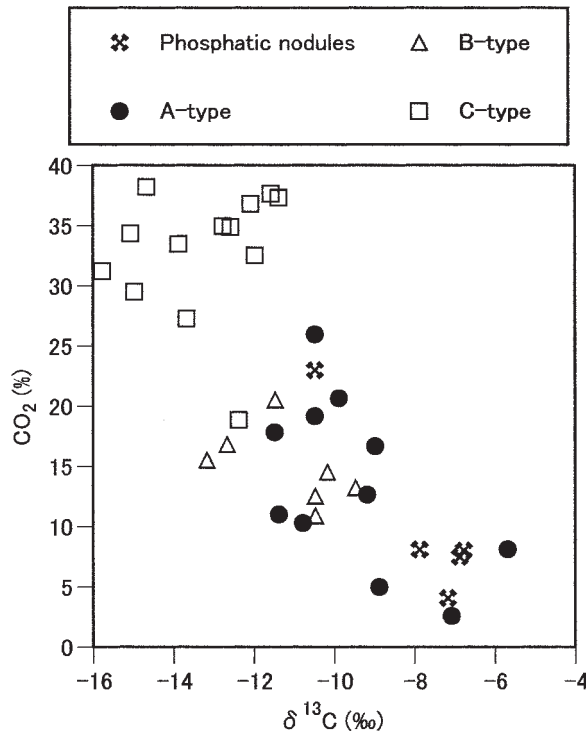


Fig. 6. Whole-rock CO₂ content plotted against calcite δ¹³C.

although the data points scatter to some extent in the high CO₂ portion of the graph.

The δ¹⁸O values for the rocks are virtually uniform regardless of the fact that the δ¹³C values vary widely. The average δ¹⁸O value of all the samples is calculated to be 15.6‰, which is lower by 2 to 12‰ than the δ¹⁸O of the Carboniferous and Permian marine limestone in the South Kitakami belt (Morikiyo et al., 1994). These data have been interpreted as indicating post-depositional oxygen isotopic alteration by ¹⁸O-depleted aqueous fluids (Morikiyo and Matsunaga, 2000).

2. Sulfur isotopes

The δ³⁴S values of pyrite and apatite, recovered from the whole-rock samples of black shale, phosphatic and carbonate rocks, are presented in Table 2 and Fig. 7, together with values reported by Endo et al. (1973) and Morikiyo et al. (1994). Isotopic analysis of sulfate ions in apatite was successful for 8 samples. For the other samples, there was too little apatite to recover sulfate ions for analysis. As seen in Fig. 7, the δ³⁴S of pyrite increases in the rocks in the following order: black shale, phosphatic nodules, A-type rock, B-type rock and phosphatic nodules with pyritiferous cores.

Black shale: The δ³⁴S of pyrite in the rock falls in the range between -41.4 and -24.3‰, except for sample 110C-1 (-9.3‰), in which pyrite is remarkably enriched

Table 2 Sulfur isotopic composition (in ‰ versus CDT) of pyrite and apatite, and the proportion of pyrite types in the black shale, phosphatic and carbonate rocks of the Toyoma Formation.

Sample No.	$\delta^{34}\text{S}$ Pyrite	$\delta^{34}\text{S}$ Apatite	$\Delta^{34}\text{S}_{\text{Ap-Py}}$	Morphology of pyrite	Locality
Black shale					
U-Sh01	-41.4			F60 M40 E0 I0	U
TM042906*	-32.7				U
276A**	-32.3			F	U
U-Sh10	-29.6			F31 M67 E2 I0	U
110C-2**	-28.4			F	T
143A**	-28.4			F>M>>E	T
KI03-2*	-26.4				U
142A**	-25.6			F	T
KI06*	-24.3				U
110C-1**	-9.3			F>>E	T
Phosphatic nodules					
KI01-4*	-21.0			F6 M42 E35 I16	U
U-N171	-20.1			F5 M68 E11 I16	U
KI01-2*	-18.7			F3 M60 E31 I6	U
Phosphatic nodules with pyritiferous core					
U-N055③	-18.3				U
U-N055②	-5.9				U
U-N055①	-5.0				U
U-N181②	-9.1			F17 M78 E5 I0	U
U-N181③	-5.8			F1 M37 E62 I0	U
U-N181④	-5.3			F1 M39 E59 I0	U
U-N181⑤	-5.0			F2 M39 E59 I0	U
U-N181⑥	-3.2			F2 M15 E83 I0	U
U-N181⑦	-3.4			F0 M17 E82 I0	U
U-N181⑧	-3.5			F2 M10 E88 I0	U
U-N181⑨	-2.9			F0 M23 E77 I0	U
U-N181⑩	-5.0			F0 M39 E61 I0	U
U-N181⑪	-5.6			F0 M93 E7 I0	U
U-N181⑫	-7.6			F20 M40 E40 I0	U
U-N011①	-6.1			F26 M74 E0 I0	U
U-N011②	-4.8			F0 M7 E93 I0	U
U-N011③	-5.3			F0 M4 E96 I0	U
U-N011④	-4.6			F0 M2 E98 I0	U
U-N011⑤	-8.1	9.6	17.7	F12 M85 E2 I0	U
U-N191bulk	-2.3	16.1	18.4		U
U-N044core	0.7	14.2	13.5		U
A-type rock					
U-A07	-22.2			F45 M25 E16 I14	U
KI02-3a*	-16.3	4.3	20.6	F38 M40 E21 I0	U
U-A03	-16.0	15.0	31.0		U
U-A11	-16.0	16.5	32.5		U
U-A01	-15.7			F23 M67 E9 I0	U
B-type rock					
U-B04	-19.3	6.5	25.8	F36 M19 E30 I14	U
U-SS14	-17.0	17.6	34.6	F8 M13 E42 I38	U
U-B07	-15.7			F0 M66 E6 I29	U
U-SS10	-12.9				U
110A**	-9.9			E	T
U-B01	-8.1			F7 M55 E7 I31	U
KT104**	-6.8			F<<E	T
U-SS04	-4.6			F12 M14 E63 I12	U
C-type rock					
276E**	-17.7			F>M>E	U
U-C11	-12.0			F5 M55 E30 I10	U

*Reproduced from Morikiyo et al. (1994).

**Reproduced from Endo et al. (1973). Abbreviations for the morphology of pyrite: F: framboidal; M: minute crystals; E: euhedral; I: irregular-shaped. Numerical values are the percentages of each pyrite type. Abbreviations for localities: U: Utatsu area; T: Toyoma area.

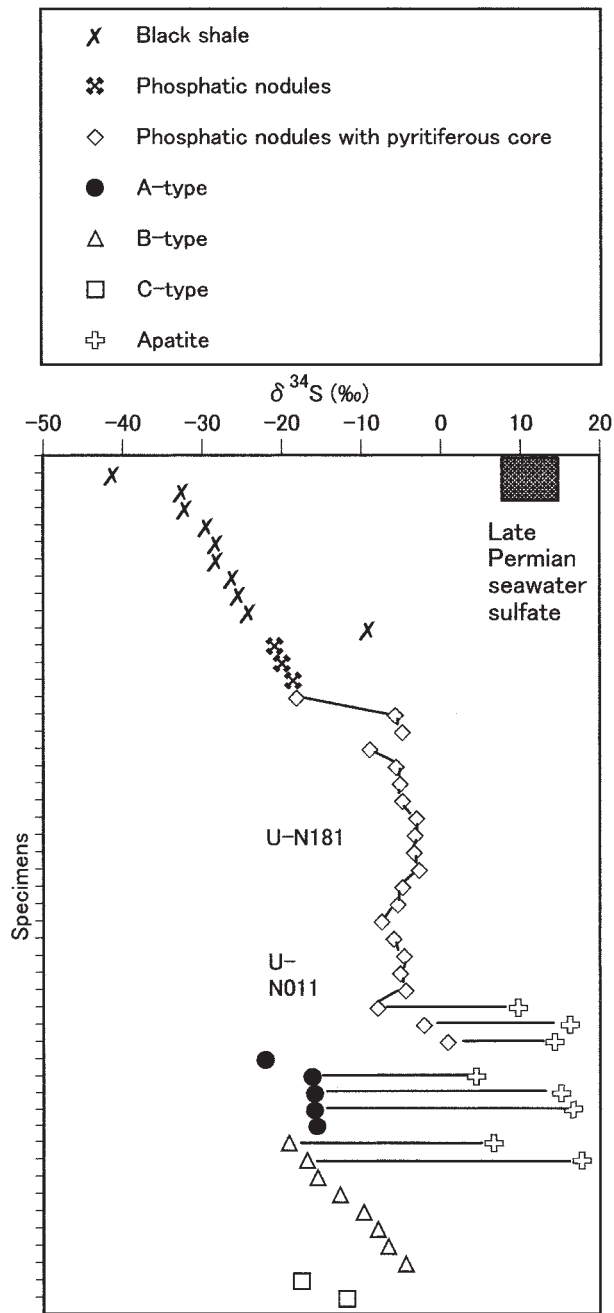


Fig. 7. Whole-rock $\delta^{34}\text{S}$ values of pyrite and apatite for black shale, phosphatic rocks, and carbonate rocks in the Toyoma Formation. Tie-lines indicate the "coexistence" of apatite and pyrite in a given sample.

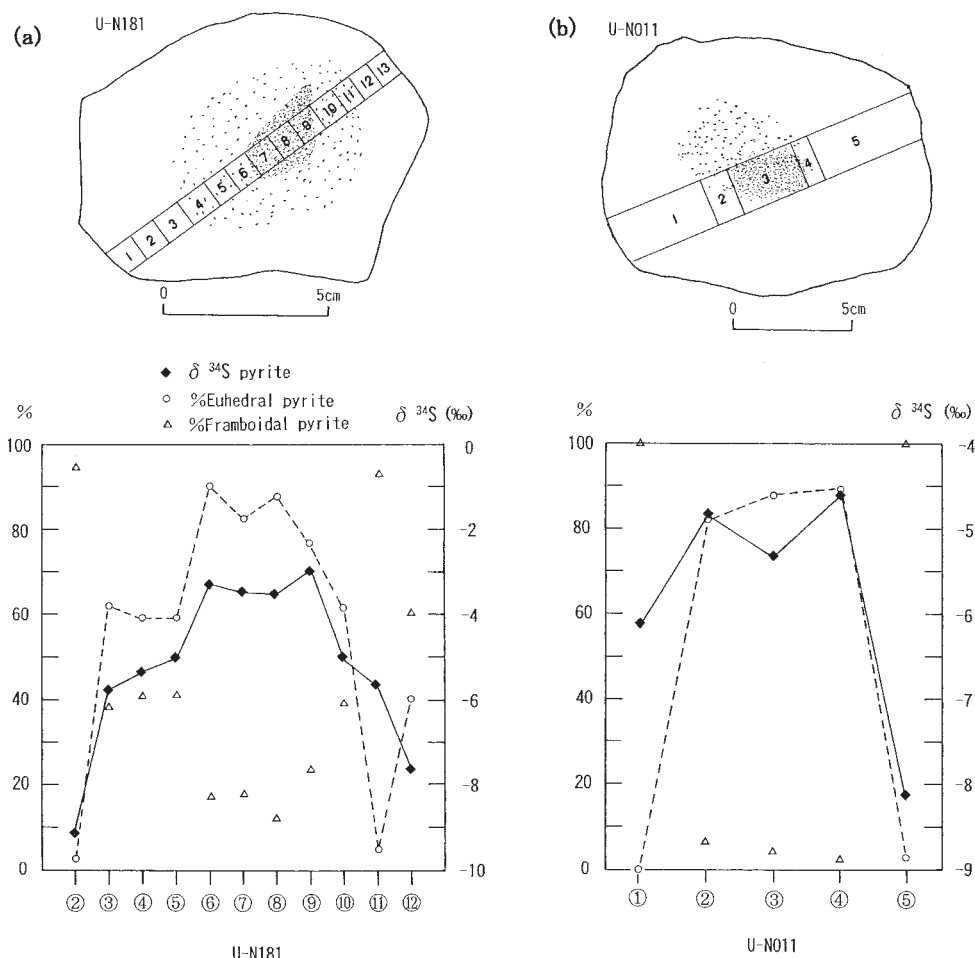


Fig. 8. Sketches of phosphatic nodules with pyritiferous cores (upper figures), a center-to-edge traverse of $\delta^{34}\text{S}$ (lower figures, right axis) and the proportion of euhedral pyrite (lower figures, left axis) for the nodules. Samples: (a) U-N181, (b) U-N011.

in ^{34}S . The marine sulfate of the Late Permian age has a $\delta^{34}\text{S}$ of about +12‰ (Strauss, 1997; Kampschulte and Strauss, 2004). Therefore, the $\delta^{34}\text{S}$ values for marine sulfate of that age and whole-rock pyrite in the black shale differ by 36 to 53‰.

Phosphatic nodules: The $\delta^{34}\text{S}$ of pyrite from the pyritiferous core-free phosphatic nodules is around -20‰. The values do not overlap with the range observed in the black shale; the pyrite in the phosphatic nodules has 4-20‰ higher $\delta^{34}\text{S}$ than the black shale. Because of sample selection failure, the $\delta^{34}\text{S}$ of sulfate ions in apatite in this rock type was not determined.

A-type: The high mode of whole-rock pyrite $\delta^{34}\text{S}$ in A-type rock appears at -16‰. Apatite in the rocks has positive $\delta^{34}\text{S}$ values ranging from +4.3 to +16.5‰. The

differences in $\delta^{34}\text{S}$ between the minerals are 20.6, 31.0 and 32.5‰.

B-type: Pyrite in B-type rocks has a $\delta^{34}\text{S}$ ranging from -19.3 to -4.6 ‰. This isotopic variation is fairly large (up to 15‰) and reflects the diversity of pyrite types in the rock. The $\delta^{34}\text{S}$ of two apatite samples were $+6.5$ and $+17.6$ ‰. The isotopic differences between “coexisting” apatite and pyrite are 25.8 and 34.6‰, similar to the values observed in A-type rock.

C-type: The $\delta^{34}\text{S}$ of pyrite in C-type rocks are -17.7 and -12.0 ‰; values similar

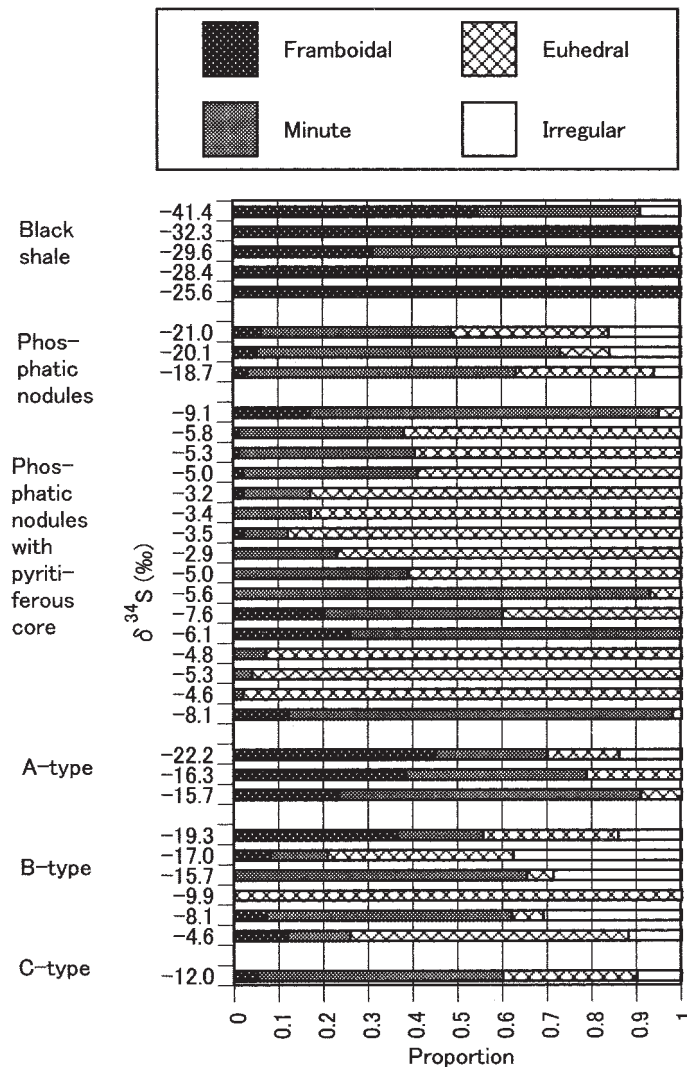


Fig. 9. Bar graphs showing the relationship between the proportions of pyrite types and rock types. The whole-rock pyrite $\delta^{34}\text{S}$ for each sample is written on the left of the bar graphs.

to A-type rock. Since C-type rock usually encloses wavy films of black shale or A-type rock (Fig. 2-3), it is likely that the pyrite analyzed was derived from fragments of these rocks in the C-type rock.

Phosphatic nodules with pyritiferous cores: Phosphatic nodules with pyritiferous cores have a zonal structure in both mineral composition and isotopic ratios. Variations of the $\delta^{34}\text{S}$ on traverses of the nodules are shown in Fig. 8a (sample: U-N181), and 8b (U-N011). The two samples show the general tendency that $\delta^{34}\text{S}$ decreases from the center to the rim. However, the isotopic profile seems to show an M-shaped figure when we examine the pattern very closely.

The $\delta^{34}\text{S}$ for “coexisting” pyrite and apatite were obtained for three samples (U-N011 ⑤, U-N191bulk, U-N044core). The $\delta^{34}\text{S}$ values of the apatite are 9.6, 16.1, and 14.2‰, respectively. These values are very similar to those for the apatite of A- and B-type rocks. The sulfur isotopic differences between apatite and pyrite for the samples are 17.7, 18.4 and 13.5‰, respectively. Compared with those observed in A- and B-type rocks, the values are notably small.

3. Pyrite types

The proportions of the pyrite types contained in the isotopically analyzed samples are shown in Fig. 9 together with their $\delta^{34}\text{S}$ values. The black shale contains exclusively framboidal and minute pyrite types and the whole-rock pyrite $\delta^{34}\text{S}$ values are very low. Scanning electron microscope (SEM) observations of the black shale revealed that some of the minute pyrite is actually small-scale framboidal pyrite.

The B-type rock of high $\delta^{34}\text{S}$ and the phosphatic nodules with pyritiferous cores are characterized by the dominance of large, euhedral pyrite. The phosphatic nodules without pyritiferous cores and A-type rocks show features and pyrite type abundances that are intermediate between the black shale and B-type rock.

4. Sulfur isotope microanalysis

The results of sulfur isotope microanalysis of the carbonate-rich phosphatic nodule KI01-4 by SIMS are presented in Table 3 and graphically shown in Fig. 11. The pyrite grains chosen for analysis are shown in Fig. 10. The $\delta^{34}\text{S}$ values of pyrite range from -51.9 to -14.5 ‰. The isotopic variation within the sample is as large as 37‰. Framboidal pyrite tends to have lower $\delta^{34}\text{S}$ values whereas large-sized pyrite has higher $\delta^{34}\text{S}$ values, as shown in Table 3.

5. Rock norms

The results of rock norm calculations are presented in Tables 4-1 to 4-3. The X values sum to nearly 1.0 (see Table 4-1) indicating that the rocks are essentially composed of the four normative minerals adopted in this study. The X values are

Table 3 Results of sulfur isotope microanalysis by the use of SIMS (Sample : carbonate-rich phosphatic nodule KI01-4).

Figure (locality)	$\delta^{34}\text{S}$ (‰)	2σ error (‰)	Description
a (13)	-51.9	0.3	Framboids associated with microcrystals forming a nebular group
b (45 edge)	-16.5	0.1	Edge of large-sized subhedral crystal
b (45 center)	-14.5	0.2	Center of large-sized subhedral crystal
b (42)	-30.6	0.1	A cluster of medium-sized euhedral crystals
b (41)	-38.2	1.3	Framboids associated with aggregates of microcrystals
c (12)	-28.6	0.3	Medium-sized euhedral crystals forming a circular structure
d (48)	-18.5	0.1	Medium-sized euhedral crystals amalgamated
whole rock	-21.0		

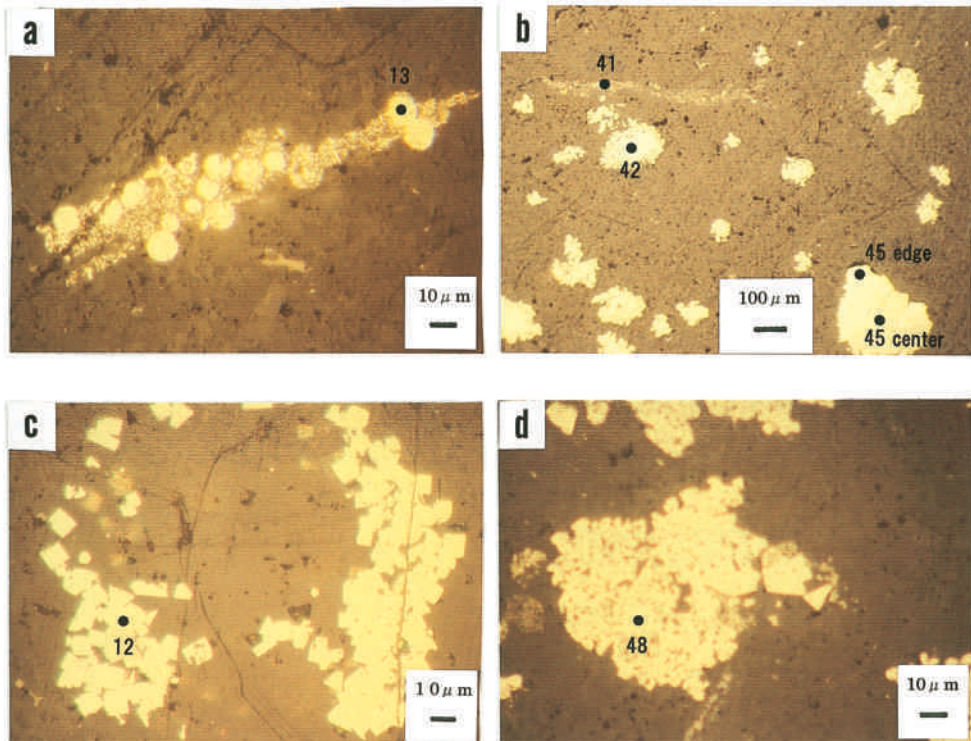


Fig. 10. Photomicrograph of sample KI01-4 showing pyrite grains analyzed using SIMS. The character of grains analyzed is described in Table 3.

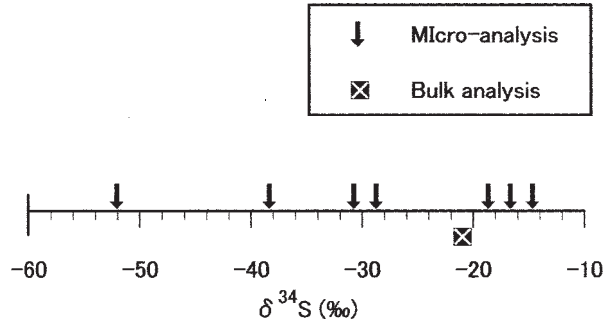


Fig. 11. Results of sulfur isotope SIMS microanalysis. (Sample KI01-4)

Table 4-1 Mole fractions for shale (X_{Shale}), pyrite (X_{Pyrite}), apatite (X_{Apatite}), and calcite (X_{Calcite}) calculated from the whole-rock chemical compositions of the rocks. Mole fractions of the samples shown in the table were calculated from total analyses.

Rock type	BS	BS	N	N	N	A	A	A	A	A	A	A	A
Specimen No.	JSL-1	JSL-2	UP-59A	UP-29 (3)	OP-1	UP-11	OP-2	OP-4	OP-3	UP-4	OP-5	UP-32	UP-20
SiO ₂	59.35	59.26	29.56	31.30	50.65	13.90	21.51	21.95	22.72	25.00	33.39	34.20	49.42
TiO ₂	0.73	0.75	0.25	0.26	0.32	0.15	0.28	0.23	0.23	0.29	0.22	0.37	0.32
Al ₂ O ₃	17.62	17.98	8.65	8.05	11.70	4.50	7.59	8.01	8.10	7.01	8.64	8.38	8.69
Fe ₂ O ₃	2.45	1.30	1.41	1.02	1.94	0.58	1.23	1.47	1.21	1.40	1.21	3.37	1.92
FeO	3.95	4.79	5.53	9.41	11.48	2.20	4.89	8.05	4.86	2.76	7.69	18.08	10.36
MnO	0.06	0.09	0.06	0.23	0.13	1.17	1.49	0.99	0.82	0.80	0.38	1.80	0.31
MgO	2.48	2.43	2.39	2.53	3.97	0.75	1.89	2.71	1.84	1.16	2.31	3.31	2.95
CaO	1.43	1.93	24.87	23.59	7.17	41.29	31.50	29.54	30.64	32.13	24.29	8.21	11.44
Na ₂ O	2.20	1.39	1.14	0.29	0.67	0.66	0.56	0.22	0.65	1.32	0.40	0.49	0.40
K ₂ O	2.85	2.93	0.71	0.06	0.67	0.56	0.79	0.31	0.58	0.77	0.26	0.81	0.21
H ₂ O+	4.00	4.27	4.76	4.53	5.54	1.89	5.22	4.21	3.39	2.47	3.58	12.43	4.07
H ₂ O-	0.63	0.33	0.15	0.04	0.05	0.08	0.07	0.04	0.13	0.09	0.04	0.97	0.05
P ₂ O ₅	0.19	0.17	17.73	13.42	4.78	5.54	1.53	5.50	12.51	3.43	9.11	4.63	2.54
F	n.d.	n.d.	1.40	0.91	0.42	0.44	0.15	0.37	0.69	0.27	0.59	0.49	0.23
CO ₂	n.d.	n.d.	1.15	4.18	0.59	26.10	20.99	16.80	11.15	20.79	7.87	2.72	6.94
Total	97.94	97.62	99.76	99.82	100.08	99.81	99.69	100.40	99.52	99.69	99.98	100.26	99.85
O=F			0.59	0.38	0.18	0.19	0.06	0.16	0.29	0.11	0.25	0.21	0.10
Total			99.17	99.44	99.90	99.62	99.63	100.24	99.23	99.58	99.73	100.05	99.75
XShale			0.498	0.528	0.854	0.234	0.363	0.370	0.383	0.422	0.563	0.577	0.833
XPyrite			0.063	0.118	0.134	0.015	0.058	0.114	0.057	0.019	0.087	0.293	0.115
XApatite			0.420	0.318	0.113	0.131	0.036	0.130	0.296	0.081	0.216	0.110	0.060
XCalcite			0.026	0.095	0.013	0.595	0.479	0.383	0.254	0.474	0.180	0.062	0.158
Total			1.007	1.059	1.115	0.975	0.935	0.998	0.991	0.996	1.046	1.041	1.167
log(XPy/XAp)			-0.824	-0.431	0.074	-0.941	0.207	-0.057	-0.715	-0.630	-0.395	0.425	0.283
δ ¹³ C(‰)				-7.2		-10.5		-9.0	-11.4	-9.9		-7.1	

Whole-rock chemical compositions of the samples reported by Kanisawa and Ehiro (1986) are reiterated here for convenience (Table 4-1 and 4-2). The procedures for the calculation of X values such as X_{Shale} are described in the Appendix. Abbreviations for rock types: N, Phosphatic nodules; A, A-type rock; B, B-type rock; C, C-type rock.

(3)

Rock type Sample No.	Sand- stone	B	B	B	B	B	B
	Av.grey -wacke	UP-42U	UP-4	UP-7	UP-43	UP-45	UP-48
FeO*	4.9	3.39	5.29	2.99	2.85	2.65	2.87
MnO	0.1	0.39	0.42	0.83	0.24	0.28	0.47
MgO	2.1	1.25	1.33	0.83	0.96	0.94	0.88
CaO	2.5	17.62	13.85	26.71	24.22	21.14	19.44
Na ₂ O	2.9	3.03	2.89	2.31	2.82	2.92	3.02
K ₂ O	2.0	1.08	1.90	0.97	0.83	0.96	0.92
P ₂ O ₅	0.2	0.27	0.22	0.18	0.16	0.14	0.14
F(ppm)		233	450	219	225	205	140
CO ₂		12.66	11.02	20.64	17.56	14.64	13.35
XSandst.		0.705	0.717	0.524	0.596	0.663	0.692
XPyrite		0	0.027	0.001	0	0	0
XApatite		0.006	0.005	0.004	0.004	0.003	0.003
XCalcite		0.289	0.251	0.471	0.401	0.334	0.305
Total		1	1	1	1	1	1
log(XPy/ XAp)		-∞	0.732	-0.60	-∞	-∞	-∞
δ ¹³ C(‰)		-10.5	-10.5	-11.5		-10.2	-9.5

(4)

Rock type Sample No.	C	C	C	C	C	C	C	C	C	C
	UP-10	UP-35	UP-59	UP-7	UP-4	UP-50	UP-63	UP-56	UP-20	UP-59 (1)
FeO*	3.00	2.64	2.43	1.68	2.41	1.13	0.98	1.31	1.31	1.43
MnO	1.09	0.69	0.80	1.39	0.93	1.39	1.15	1.49	0.86	1.61
MgO	0.93	0.74	0.96	0.59	0.54	0.35	0.47	0.51	0.61	0.55
CaO	34.30	38.21	36.54	40.55	47.53	48.34	48.72	46.61	48.53	45.44
Na ₂ O	1.01	0.97	0.98	0.59	0.64	0.46	0.34	0.56	0.42	0.64
K ₂ O	1.22	0.99	1.01	0.91	0.54	0.36	0.35	0.48	0.55	0.43
P ₂ O ₅	0.18	0.15	0.11	0.07	0.13	0.12	0.12	0.08	0.07	0.09
F(ppm)	250	207	187	168	134	126	103	129	104	85
CO ₂	27.41	29.63	28.97	32.66	35.10	37.79	38.35	37.46	37.89	36.95
XShale	0.365	0.317	0.337	0.253	0.184	0.135	0.122	0.144	0.134	0.155
XPyrite	0.006	0.004	0	0	0.012	0	0	0	0	0
XApatite	0.004	0.004	0.003	0.002	0.003	0.003	0.003	0.002	0.002	0.002
XCalcite	0.625	0.676	0.661	0.745	0.801	0.862	0.875	0.854	0.864	0.843
Total	1	1	1	1	1	1	1	1	1	1
log(XPy/ XAp)	1.5	0	-∞	-∞	0.602	-∞	-∞	-∞	-∞	-∞
δ ¹³ C(‰)	-13.7	-15.0		-12.0	-12.8	-11.6	-14.7	-11.4		-12.1

Table 4-3 Major and trace element contents obtained by ICP-MS analysis.

Rock type	N	N	N	N	N	N	A	A	A	A	Shale with scale fossils
Sample No.	U-N181 b	U-N171 b	U-N011 b	U-N044 core	890429 01-2	921002 09b	890429 02-3a	U-A01	U-A03	U-A11	080618 07
SiO ₂	47.2	23.9	42.3	49.6	19.85	18.9	29.1	48.4	40.1	41.9	72.4
TiO ₂	0.48	0.26	0.24	0.21	0.18	0.18	0.3	0.62	0.44	0.42	0.44
Al ₂ O ₃	11.15	6.73	6.50	4.74	5.08	5.13	7.88	14.75	11.8	11.0	10.4
Fe ₂ O ₃ *	7.73	6.72	16.1	20.3	6.8	5.82	6.46	15.2	7.94	9.44	3.15
MnO	0.22	1.16	0.5	0.41	1.17	0.8	0.64	0.26	0.38	0.48	0.02
MgO	2.1	1.45	2.29	2.08	1.16	1.16	1.6	3.14	2.21	2.02	0.96
CaO	12.85	31.6	16.5	6.92	34.8	35.5	27.4	4.86	15.95	15.75	2.25
Na ₂ O	1.05	1.98	0.25	0.36	0.59	0.80	0.99	1.66	1.20	1.20	1.1
K ₂ O	1.55	0.20	0.16	0.48	0.45	0.44	0.74	1.24	1.55	1.15	1.56
P ₂ O ₅	7.97	3.17	2.77	0.43	5.59	5.36	4.41	0.31	5.47	2.3	0.31
LOI	6.33	23.4	10.55	12.45	24.5	24.7	20.0	8.50	11.05	13.35	7.13
CO ₂ calculated	(3.04)	(21.73)	(7.60)	(8.99)	(23.11)	(23.38)	(17.97)	(5.12)	(8.25)	(10.43)	
Total	98.63	100.57	98.16	97.98	100.17	98.79	99.52	98.94	98.09	99.01	99.72
XShale	0.796	0.403	0.713	0.836	0.335	0.319	0.491	0.816	0.676	0.706	
XPyrite	0.035	0.054	0.168	0.218	0.062	0.049	0.043	0.144	0.049	0.068	
XApatite	0.189	0.075	0.066	0.010	0.132	0.127	0.104	0.007	0.130	0.054	
XCalcite	0.069	0.496	0.173	0.205	0.527	0.533	0.410	0.117	0.188	0.238	
Total	1.089	1.028	1.120	1.269	1.056	1.028	1.047	1.085	1.043	1.066	
log(XPy /XAp)	-0.732	-0.143	0.406	1.338	0.470	-0.414	-0.384	1.313	-0.424	0.100	
δ ¹³ C(‰)			-6.9		-10.5		-11.5	-8.9	-5.7	-10.8	
REE(ppm)											
Y	299	169	244	31.8	298	315	180	30.1	181.5	77.1	24.6
La	137.5	63.2	84.4	14.2	102	124	67.3	28.1	77.3	43.4	21.5
Ce	363	145	227	37.3	253	270	169	58.8	279	105.5	53.5
Pr	48.4	19.05	30.7	4.87	30.7	36.3	24.4	7.14	49.2	14.05	6.32
Nd	233	96.8	156	24.5	140.5	165	114	28.7	241	62.2	25.3
Sm	54.3	22.1	38.2	7.32	26.6	37.8	28.4	6.19	55.4	14.3	5.81
Eu	28.6	6.41	14.35	7.94	13	13.25	12.4	1.61	12.95	4.83	1.32
Gd	68.4	29.4	49.6	8.11	42.3	55.4	37.7	6.41	59.9	17.45	5.6
Tb	10	4.51	7.67	1.24	6.38	8.11	5.36	0.96	7.98	2.49	0.83
Dy	51.9	25.3	42.4	6.52	38.5	45.1	28.5	5.79	37.6	13.4	4.82
Ho	8.87	4.58	7.24	1.1	7.39	7.76	4.8	1.14	5.79	2.3	0.87
Er	17.2	9.01	14.05	2.43	14.15	16.9	11.15	3.48	12.5	5.75	2.42
Tm	1.72	0.96	1.42	0.33	1.29	1.48	1.07	0.5	1.12	0.65	0.34
Yb	7.42	4.29	5.9	1.78	4.84	6.97	5.95	3.58	6.16	3.84	2.16
Lu	1	0.61	0.74	0.27	0.58	0.85	0.76	0.51	0.82	0.58	0.3

* Total Fe as Fe₂O₃

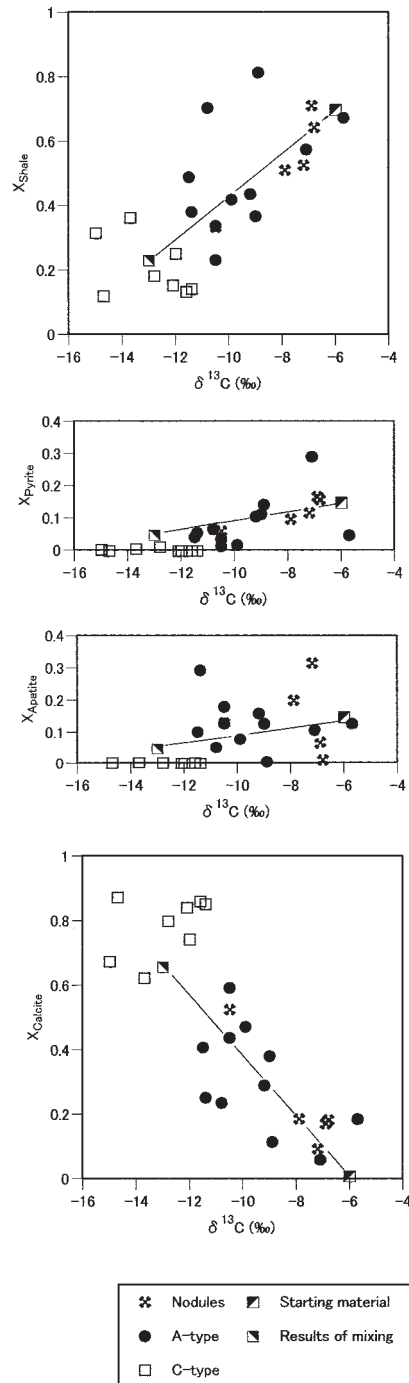


Fig. 12. Plot of X values against $\delta^{13}\text{C}$ of calcite for phosphatic nodules and A-, B- and C-type rocks. Top: Plot of X_{Shale} . Second: X_{Pyrite} . Third: X_{Apatite} . Bottom: X_{Calcite} .

plotted against $\delta^{13}\text{C}$, as shown in Fig. 12.

$X_{\text{Shale}} : X_{\text{Shale}}$ is high ($X_{\text{Shale}}=0.7$) at the right portion of the diagram where $\delta^{13}\text{C}=-6$ to -7‰ . With the decrease in $\delta^{13}\text{C}$, X_{Shale} declines, reaching values of 0.1 to 0.3 at $\delta^{13}\text{C}=-15\text{‰}$.

$X_{\text{Pyrite}} : X_{\text{Pyrite}}$ is highest at $\delta^{13}\text{C}=-6$ to -7‰ . As $\delta^{13}\text{C}$ decreases, X_{Pyrite} decreases. It approaches 0 when $\delta^{13}\text{C}$ is about -12‰ . X_{Pyrite} is 0 when $\delta^{13}\text{C}=-12$ to -15‰ .

$X_{\text{Apatite}} : X_{\text{Apatite}}$ values are widely scattered. However, the overall tendency of X_{Apatite} is to decrease with decreasing $\delta^{13}\text{C}$. X_{Apatite} ranges from 0 to 0.3 at $\delta^{13}\text{C}=-6$ to -7‰ . X_{Apatite} approaches 0 at $\delta^{13}\text{C}=-12\text{‰}$.

$X_{\text{Calcite}} : X_{\text{Calcite}}$ ranges from 0.05 to 0.2 on the right of the diagram ($\delta^{13}\text{C}=-6$ to -7‰). Then, as $\delta^{13}\text{C}$ decreases, X_{Calcite} clearly increases, reaching about 0.8 at $\delta^{13}\text{C}=-15\text{‰}$. In the region where the $\delta^{13}\text{C}$ value is lower than -12‰ , X_{Pyrite} and X_{Apatite} are virtually 0 and X_{Calcite} is 0.65 to 0.85.

VI Discussion

1. Cause of $\delta^{34}\text{S}$ variation in pyrite

The results of sulfur isotope microanalysis using secondary ion mass spectrometry (SIMS) of pyrite in the carbonate-rich phosphatic nodule of sample KI01-4 are shown in Fig. 11. The $\delta^{34}\text{S}$ of pyrite is found to vary from -51.9 to -14.5‰ , varying as much as 37‰ . Thus, the sample contains various pyrites having different $\delta^{34}\text{S}$ values. The $\delta^{34}\text{S}$ of pyrite from a whole-rock sample analyzed using the conventional method is -21.0‰ . Thus it is clear that the $\delta^{34}\text{S}$ obtained by conventional analysis is an averaged value, which depends on both the proportion of pyrite types, each of which has a different $\delta^{34}\text{S}$, and the extent of $\delta^{34}\text{S}$ variation shown by all the pyrite in a sample.

The lowest $\delta^{34}\text{S}$ of pyrite found in KI01-4 is -51.9‰ , and the second lowest is -38.2‰ . These pyrites are framboidal. The $\delta^{34}\text{S}$ of sulfate ion in Late Permian seawater obtained from the study of evaporites is from $+8$ to $+14\text{‰}$ (Nielsen, 1978 ; Claypool et al., 1980 ; Nathan and Nielsen, 1980 ; Strauss, 1997). A study of structurally substituted sulfate in carbonates shows that it is about $+12\text{‰}$ (Kampschulte and Strauss, 2004).

The extent of sulfur isotope fractionation in microbial sulfate reduction, deduced from the $\delta^{34}\text{S}$ of seawater sulfate and that of pyrite in the marine sediments, ranges from 30 to 70‰ (Fig. 5 of Canfield (2001)). Thus, it is reasonable to think that the framboidal pyrite in sample KI01-4, which shows a $\delta^{34}\text{S}$ of -51.9 to -38.2‰ , is the product of microbial sulfate reduction from Late Permian seawater sulfate of about $+12\text{‰}$.

Some of the phosphatic nodules carry calcite whose $\delta^{13}\text{C}$ is lower than that of

marine limestone ($\delta^{13}\text{C}$ of phosphatic nodules : -10.5 to -6.8% , Fig. 5). The calcite in the A-, B- and C-type rocks has a much lower value than the phosphatic nodules. This indicates the incorporation of carbon of organic matter origin into the calcite, which supports the view that sulfate reduction occurred in the sediments of the Toyoma Formation.

It is conceivable that the $\delta^{34}\text{S}$ variation among individual pyrite grains in KI01-4 was the result of Rayleigh fractionation upon pyrite precipitation from the pore water. Since the magnitude of sulfur isotope fractionation between sulfate and sulfide is very large, the precipitation of pyrite from the pore water in a closed system will raise the $\delta^{34}\text{S}$ of sulfate in the water. Provided the isotope fractionation between sulfate and sulfide is nearly constant throughout sulfate reduction, the $\delta^{34}\text{S}$ of pyrite increases with the progress of pyrite precipitation (Hoefs, 1987). However, the extent of the fractionation is controlled by various factors such as the physiology of the bacteria, the temperature, the rate of sulfate reduction, the concentration of sulfate in the system, and the size of the sulfate reservoir (Longstaffe, 1989). Thus the possibility remains that a change in the kinetic factors listed above produced the isotopic variation observed in KI01-4 with a constant interstitial water sulfate $\delta^{34}\text{S}$.

The $\delta^{13}\text{C}$ of calcite decreases in the rocks in the following order : phosphatic nodules, followed by A-, B- and C-type rocks as seen in Fig. 5. The whole-rock pyrite $\delta^{34}\text{S}$ values, on the contrary, are higher but in the same order (Fig. 7) when we exclude the data of the phosphatic nodules having pyritiferous cores. Although the whole-rock pyrite $\delta^{34}\text{S}$ values are averages, they must reflect the proportions of the pyrite types, each of which has a different $\delta^{34}\text{S}$ from the others. If this is the case, the fact that the whole-rock $\delta^{34}\text{S}$ is high indicates the dominance of a high- $\delta^{34}\text{S}$ pyrite type in a sample. Therefore, when the carbon isotopic features are taken into consideration, it is reasonable to conclude that the increase in pyrite $\delta^{34}\text{S}$ is due to the progress of sulfate reduction in closed sediments in a manner such as Rayleigh fractionation.

2. Phosphatic nodules

(1) Source of phosphorus

The concentrations of Yttrium (Y), Lanthanum (La), and Cerium (Ce) in the phosphatic rocks of the Toyoma Formation are exceedingly high. The sample UP-59A (P_2O_5 contents 17.73%) contains 837 ppm of Y and 956 ppm Ce (Kanisawa et al., 1985). According to the summary in Kolodny (1981), the Ce content of the world's phosphorite is from 80 to 260 ppm. Thus the phosphatic rocks in the Toyoma Formation seem to be peculiar in their rare earth element (REE) contents. The concentrations of Y, La and Ce in the rocks are proportional to the P_2O_5 concentration, as shown in Fig. 13. The North American Shale Composite (NASC)-normalized values of rare earth elements in

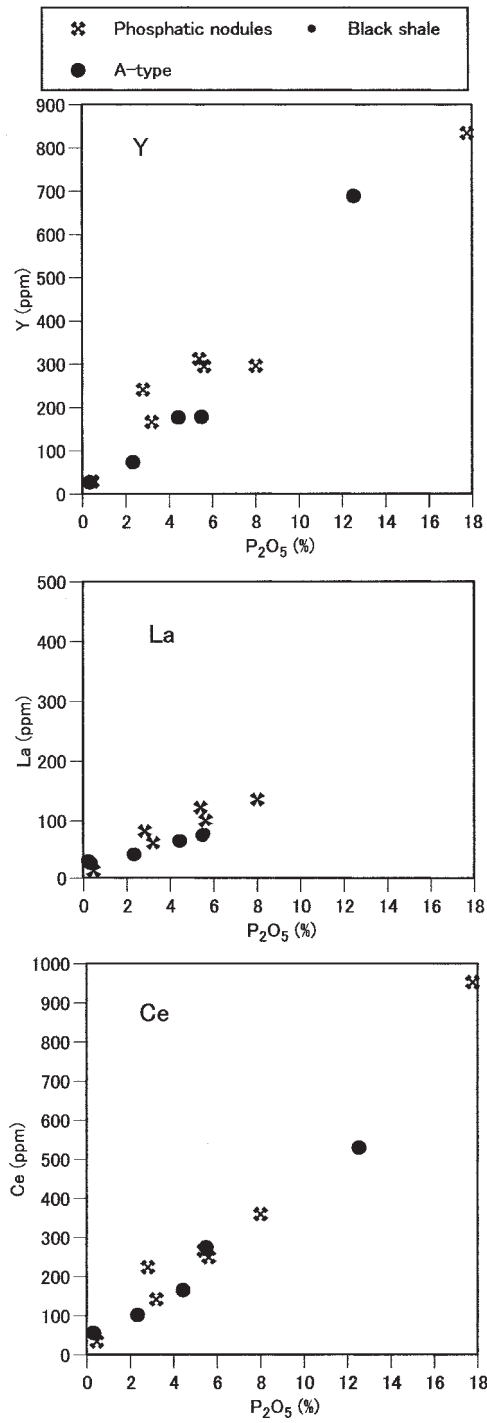


Fig. 13. Plot of whole-rock Y, La and Ce content (ppm) against P_2O_5 content (%). Top: Y content. Middle: La. Bottom: Ce.

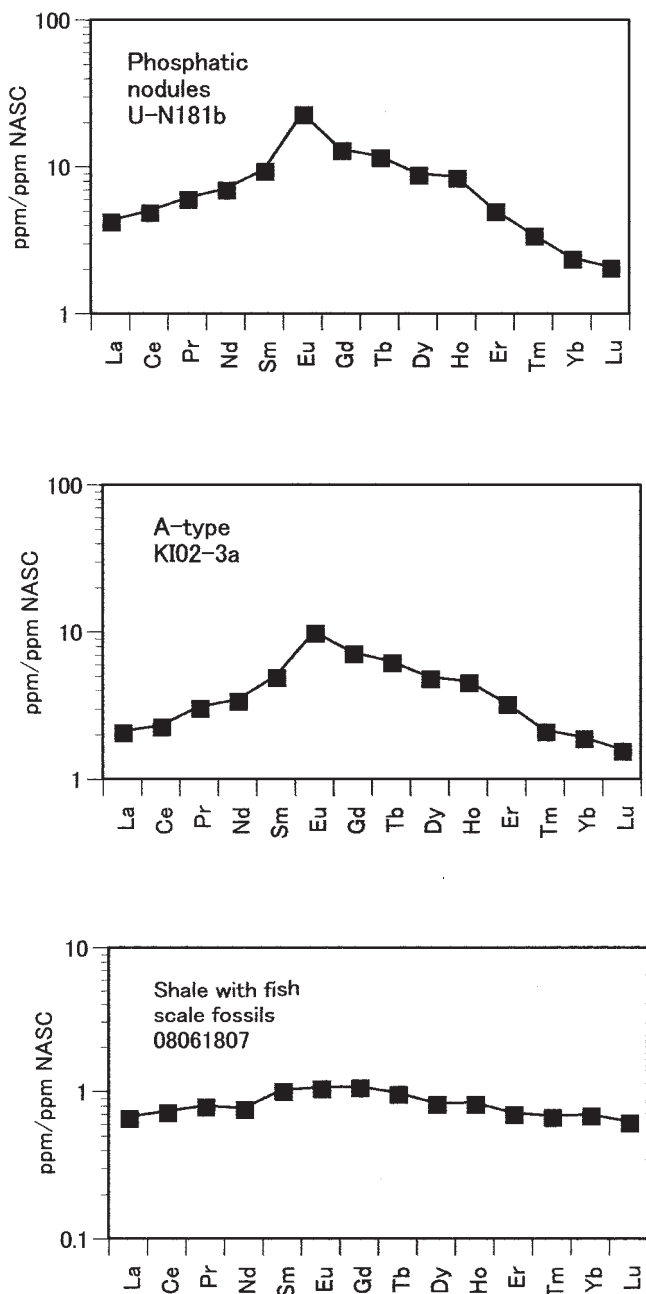


Fig. 14. NASC-normalized rare earth pattern of the phosphatic nodule and A-type rock. Top : Phosphatic nodule (sample U-N181b). Middle : A-type rock (sample KI02-3a). Bottom : Composite sample of shale and fossils of fish scales from the Tertiary Bessho Formation.

the phosphatic rocks from the Toyoma Formation show relative enrichment in the middle rare earth elements with a peak at Europium (Eu), showing a mountain-like pattern (Fig. 14). A similar pattern, although the enrichment is minute, is recognized for the shale sample containing abundant fish scale fossils collected from the Tertiary Bessho Formation of Nagano prefecture (Fig. 14).

It is well known that fish bones, scales and teeth deposited on the ocean floor are enriched in rare earth elements owing to ion exchange reactions with seawater. The NASC-normalized rare earth pattern of ichthyoliths exhibits maximum enrichment at the middle rare earth elements such as Eu, Gadolinium (Gd) and Dysprosium (Dy) (Fig. 6 and 8 of Elderfield and Pagett, 1986), which is similar to the REE pattern of the phosphatic rocks of the Toyoma Formation. Thus, we conclude from the distribution pattern of rare earth elements that the source of the phosphatic rocks of the Toyoma formation is not organically bound phosphorus but biogenic phosphate debris deposited on the ocean floor.

The view that rare earth elements in the apatite could have been accommodated after the precipitation of the mineral through reaction with seawater is hardly acceptable. Because the phosphatic rocks in the Toyoma Formation were formed within the sediments diagenetically as described below, the apatite was not under fresh seawater but under pore water. The pore water, insulated from the seawater of a marine reservoir, does not contain enough rare earth elements to produce the observed rare earth element contents of the phosphatic rocks.

(2) The site of phosphatic nodule formation

The phosphatic nodules were formed within sediments after deposition. This view is derived from the following observations.

a) Even the phosphatic nodule having the highest P_2O_5 content (sample UP-59A) contains a mole fraction of shale of 0.498 (49.8 mole%). This indicates that the precipitation of apatite occurred within the sediments in such a manner as to fill the interstices of the pelitic sediments.

b) Some of the phosphatic nodules carry calcite. In those cases its $\delta^{13}C$ is from -10.5 to -6.8% . The $\delta^{13}C$ values indicate the precipitation of calcite from closed interstitial water in which the $\delta^{13}C$ of dissolved hydrogencarbonate ion is low due to the oxidation of organic matter.

From these facts, it seems to be indisputable that apatite in the phosphatic nodules was not precipitated directly from seawater at the bottom of sea but was precipitated diagenetically within the sediments after deposition.

(3) The period of phosphatic nodule formation

The phosphatic nodules were formed and consolidated at the shallowest portion

within the sediment column in all the rocks of the Toyoma Formation. This is known from the following observations :

a) Microbial sulfate reduction occurred within the sediments of the Toyoma Formation (Endo et al., 1973 ; Morikiyo et al., 1994). However the apatite in both the phosphatic nodules and A-type rock contains sulfate ions in its lattice. This indicates that the apatite was not precipitated from the interstitial water, as has been advanced, since sulfate ion is depleted in the process of sulfate reduction.

b) The $\delta^{34}\text{S}$ of sulfate in apatite is around +12‰ (average of 8 data points), which is similar to that of sulfate in Late Permian seawater. In Rayleigh fractionation, the $\delta^{34}\text{S}$ of sulfate ion in interstitial water is expected to rise with the progress of pyrite precipitation. The fact that the apatite $\delta^{34}\text{S}$ does not differ from that of Late Permian seawater suggests that the interstitial water was not evolved.

c) The whole-rock pyrite $\delta^{34}\text{S}$ values of the phosphatic nodules are the lowest among the four rocks of diagenetic origin in the Toyoma Formation. Although the isotopic ratios obtained are averaged values for all pyrite types, the isotopic signatures of the phosphatic nodules are interpreted as showing low- $\delta^{34}\text{S}$ type pyrite to be dominant. The occurrence of low- $\delta^{34}\text{S}$ pyrite also indicates that the interstitial water was not evolved.

d) Some of the phosphatic nodules, especially those having high concentrations of P_2O_5 , are composed of pyrite, apatite and clastic materials (shale components), while calcite is virtually lacking (See Table 4-1, 4-2). As described before, the mole fraction of normative calcite in a rock, X_{Calcite} , increases as $\delta^{13}\text{C}$ decreases (Fig. 12). Lower $\delta^{13}\text{C}$ for calcite means calcite precipitation occurred in deeper locations (Irwin et al., 1977 ; Hennessy and Knauth, 1985). From the tendency exhibited by X_{Calcite} versus $\delta^{13}\text{C}$ in Fig. 12, the fact that calcite is virtually lacking in some of the nodules indicates that the site of phosphatic nodule formation was within shallow sediments.

e) The highest $\delta^{13}\text{C}$ values of all of the rocks in the Toyoma Formation are those of the calcite-bearing phosphatic nodules. This is due to the high proportions of hydrogen-carbonate ion of marine reservoir origin in the interstitial water, indicating that calcite precipitation occurred at shallow burial depths.

From these lines of evidence, it is indisputable that the apatite in the phosphatic nodules precipitated in very shallow portions of the Toyoma Formation sediment column. Pyrite in the nodules also precipitated at similar depths of burial leading to the complete consolidation of the nodules of calcite-lacking type.

(4) The cause of apatite precipitation

The conclusions that the source of phosphorus is biogenic phosphate debris deposited on the ocean floor and that the apatite in the phosphatic nodules precipitated at the shallowest portion within the sediment column lead logically to the following

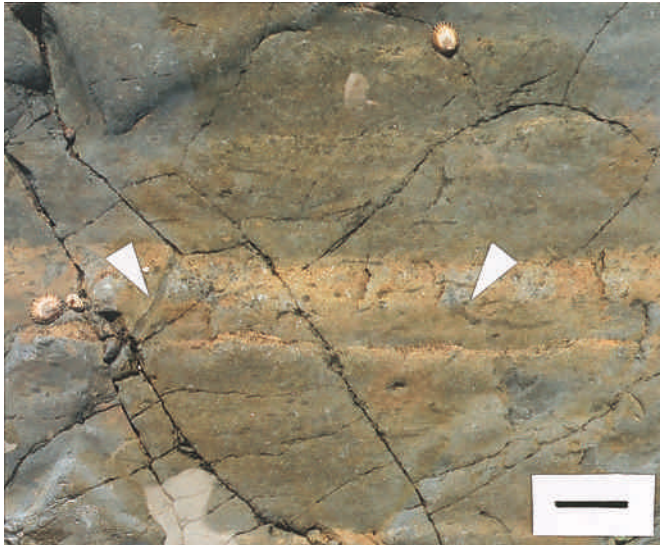


Fig. 15. Trace fossils (burrows) observed in the mudstone bed of the Suenosaki Formation. Scale bar is 5 cm long.

scenario : The biogenic phosphate debris dissolved after deposition. Subsequently, apatite precipitated from the interstitial water in the sediment. The central problem is what kind of geological-chemical process brought about the dissolution and subsequent precipitation of apatite.

There have been recent reports of corrosion of the concrete walls of several sewer systems in Japan. This resulted from the action of sulfuric acid, produced by the chemosynthesis of sulfur-oxidizing bacteria such as *Thiobacillus* (Yamanaka et al., 2002). Because the atmosphere in the sewer systems contains molecular oxygen and hydrogen sulfide, the latter of which is produced by sulfate-reducing bacteria in sewage, sulfur-oxidizing bacteria began to reside in the walls of the system. Molecular oxygen must be present in order for the bacteria to grow.

Trace fossils such as burrows occur in the black shale of the Toyoma Formation (Kamada, 1993, 1998). An example is shown in Fig. 15. From this, it can be recognized that the ocean floor on which sediments of the Toyoma Formation were deposited was not anoxic but oxic. On the other hand, sediments inside were anoxic, producing conditions that would allow microbial sulfate reduction to proceed.

From the conditions described above, we come to understand that the following conditions existed in the surface sediments :

a) Hydrogen sulfide produced in the anoxic sediments inside diffused upward to the oxic surface sediments (Fig. 16). Because of the presence of molecular oxygen, sulfur-oxidizing bacteria such as *Beggiatoa* or *Thioploca* began to grow in the surface sediment. Then sulfuric acid was produced according to the reaction :

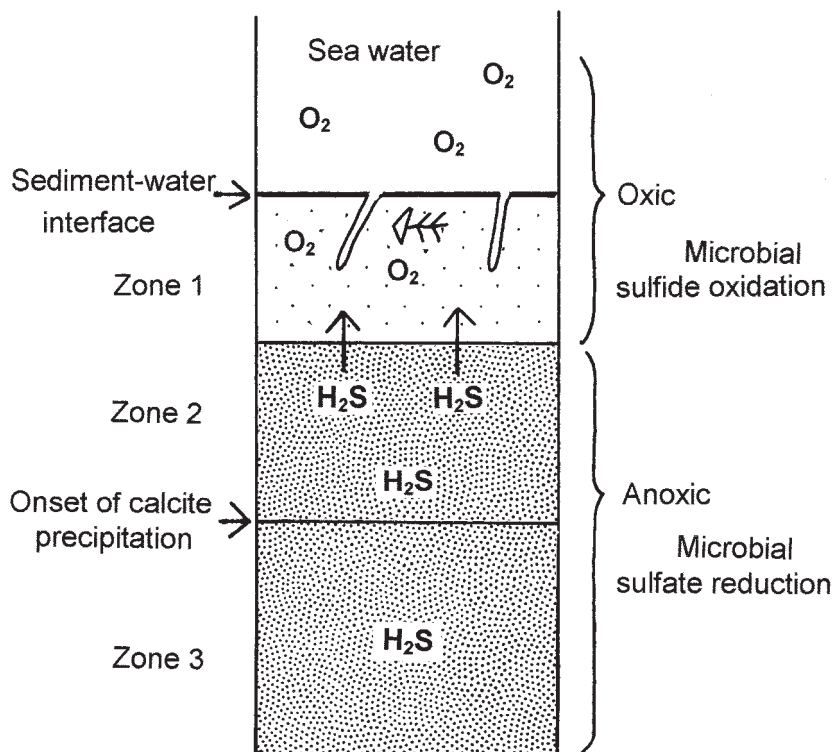
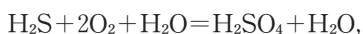
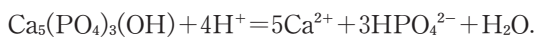


Fig. 16. The inferred section around the seawater/sediment interface in the Toyoma sedimentary basin.

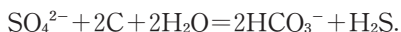


resulting in the dissolution of the biogenic phosphate debris in the sediments. The equation of phosphate dissolution may be like this:

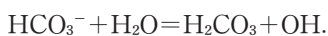


Thus the concentration of total phosphate ions in the interstitial water was raised.

b) As time passed, new clastic materials were deposited on the sea bottom. Because of this, the former oxic surface sediment layer was overlain by new sediments and became anoxic. Strict anaerobic sulfate-reducing bacteria replaced the sulfur-oxidizing bacteria, initiating sulfate reduction. According to Berner (1971), the chemical process of sulfate reduction is as follows:



The alkalinity of the interstitial water increases as the reaction progresses because SO_4^{2-} ions in the interstitial water are consumed. The increase in alkalinity raises the concentrations of total carbonate ions and also results in the rise of pH according to the reaction:



c) Because of these reactions, HPO_4^{2-} ion in the water was transformed to PO_4^{3-} . The rise of total phosphate ions in the interstitial water due to the dissolution of biogenic phosphate debris as well as the increase in pH results in the super saturation of fluorapatite components in the water. Thus apatite began to precipitate forming the phosphatic nodules and other phosphatic rocks (i.e., A-type rock).

3. Diagenetic zones

It is essential to establish a way to measure the progress of diagenesis in order to describe the formative process of phosphatic nodules and A-, B- and C- type rocks. For this purpose, the diagenetic zones in which specific authigenic minerals were precipitated are defined. The spatial distribution of the diagenetic zones in the sediment column is shown in Fig. 16.

(1) Zone 3

It is well known that the $\delta^{13}\text{C}$ of dissolved carbon dioxide in pore water decreases with increasing sediment burial owing to the progress of oxidation of organic matter in sediments (Irwin et al., 1977; Hennessy and Knauth, 1985). There is sufficient evidence to prove that sulfate reduction occurred in the sediments of the Toyoma Formation, as has already been described. Therefore, it is possible to utilize the $\delta^{13}\text{C}$ of calcite as the numerical measure for the progress of sediment burial where calcite is present in rocks. However, it should be noticed that the $\delta^{13}\text{C}$ values of calcite obtained in this study were from the total rock and that the $\delta^{13}\text{C}$ values, like the case of whole-rock pyrite $\delta^{34}\text{S}$, are the averaged value of the $\delta^{13}\text{C}$ of individual calcites.

The CO_2 content of the rocks increases as $\delta^{13}\text{C}$ decreases, as seen in Fig. 6. Thus the X_{Calcite} rises, whereas the X_{Shale} falls as $\delta^{13}\text{C}$ decreases (Fig. 12). This relation is interpreted as being due to the addition of calcite to the precursor rocks with as sediment burial progressed. Because of this, initial clastic material (the shale component) was diluted with calcite. Now let us consider the case in which calcite having a $\delta^{13}\text{C}$ of -13‰ is added to a model precursor rock consisting of 0.7 mole of shale, 0.15 mole of pyrite, 0.15 mole of apatite and 0.01 mole of calcite. The $\delta^{13}\text{C}$ of calcite in the rock is assumed to be -6‰ . The result of adding 2 moles of calcite to the precursor rock is shown in Fig. 12. The lines depicted in Fig. 12 represent the effect of calcite incorporation to the precursor rock. With the exception of X_{Apatite} , the data points are distributed near the line. From this, it is concluded that the precipitation of calcite and its incorporation to the precursor rock progressed as sediment burial increased. Considerable scattering is seen in the case of X_{Apatite} . This may be ascribed to inappropriate mineral composition of the model precursor rock. Precursor rocks must have possessed variable pyrite : apatite ratios before calcite incorporation.

A question arises from these considerations. Were apatite and pyrite not

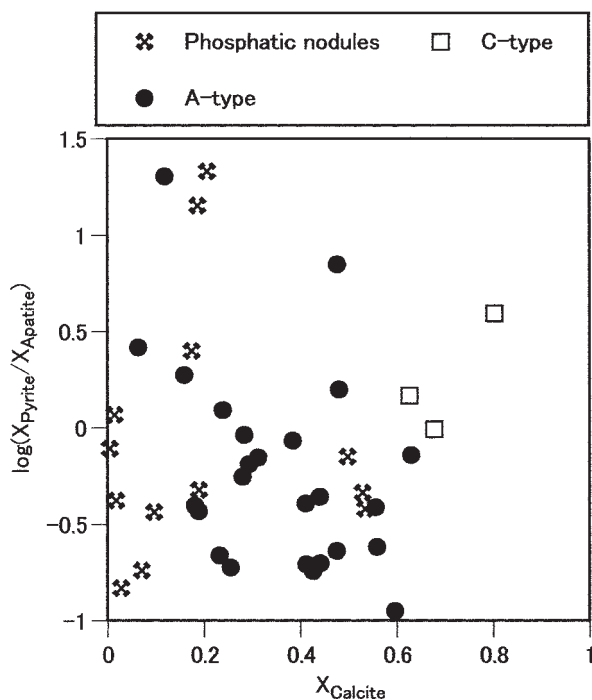


Fig. 17. Plot of $\log(X_{\text{Pyrite}}/X_{\text{Apatite}})$ values against X_{Calcite} .

precipitated and incorporated into the precursor rock during the period of calcite precipitation? In order to examine this problem, a diagram showing the relation between $X_{\text{Pyrite}}/X_{\text{Apatite}}$ and X_{Calcite} is constructed (Fig. 17). Since the ratio of $X_{\text{Pyrite}}/X_{\text{Apatite}}$ varies greatly, the logarithm of the ratio was taken and plotted in the diagram. The data points scatter widely in the diagram and no systematic variation of $X_{\text{Pyrite}}/X_{\text{Apatite}}$ with X_{Calcite} is seen. This indicates that the proportions of pyrite to apatite in precursor rocks had been set before the incorporation of calcite to the rocks took place. Since there is a clear relation between CO_2 content and $\delta^{13}\text{C}$ (Fig. 6), the depth of burial in which calcite incorporation took place is deduced (i.e. the depth at which the $\delta^{13}\text{C}$ of calcite is about -6‰). Below that depth, the only authigenic mineral incorporated into the precursor rock as sediment burial progressed was calcite. The inference is supported by the field occurrence and chemical composition of the C-type rock. As described before, some of the C-type carbonate rock occurs as veins penetrating black shale (Fig. 2-5) indicating that it was formed from aqueous solution. Since the amounts of pyrite and apatite contained in C-type rock are very small, the solution must have been depleted in pyrite and apatite components. From the facts described above, it can be inferred that the interstitial water became carbonate-dominant and sulfide- and phosphate-depleted at a relatively advanced stage of early

diagenesis. The burial depth in which only calcite precipitates from the interstitial water is defined as Zone 3.

(2) Zone 2

The tendency for X_{calcite} to decrease with a rise in $\delta^{13}\text{C}$ is seen clearly in Fig. 12. The X_{calcite} is about 0.7 to 0.9 at $\delta^{13}\text{C}$ values of -15 to -12‰ but about 0.1 to 0.2 at $\delta^{13}\text{C}$ values of -8 to -6‰ . We did not obtain any calcite-bearing sample with a $\delta^{13}\text{C}$ higher than -5.7‰ . From this, we infer that calcite could not be precipitated from the interstitial water in sediments shallower than the depth at which the $\delta^{13}\text{C}$ of dissolved carbonate is -5.7‰ .

Pyrite and apatite, on the other hand, must have already precipitated above that depth. This inference is based on the following observations: The X_{pyrite} and X_{apatite} increase with increasing $\delta^{13}\text{C}$ (Fig. 12). Carbonate-free phosphatic nodules do occur (Samples: OP-1, UP-59C, UP-17, see Table 4-1 and 4-2). Carbonate-free samples cannot be shown in the X_{mineral} vs $\delta^{13}\text{C}$ diagram because calcite is lacking. The range of burial depth in which authigenic pyrite and apatite precipitate but calcite does not is defined as Zone 2.

(3) Zone 1

The seawater in the Toyoma sedimentary basin is assumed not to be anoxic, judging from the following observations:

- a) Sediments are frequently bioturbated and burrowers are found (Kamada, 1993, 1998). The example of trace fossils observed is shown in Fig. 15. The presence or absence of burrowers is one of the fundamental criteria used to determine whether environments are oxic or anoxic (Wignall, 1994).
- b) The Uranium (U) and Thorium (Th) content of the black shale (U=0.8 to 3.9 ppm) are much lower than that in black shale deposited in reduced seawater (Kanaya and Katada, 1975).
- c) The MnO content of the phosphatic nodules and A-type rock (0.22 to 1.80%) is remarkably high compared to black shale (0.03-0.12%). The MnO content of clastic silicate minerals is usually very low and the minerals are not decomposable during early diagenesis. Thus the MnO contained in the phosphatic nodules and A-type rock was not derived from clastic silicate minerals but must have originated from manganese oxide or hydroxide precipitated from seawater. Formation of manganese oxide or hydroxide requires oxic conditions. Thus we conclude that only deposits below the water/sediment interface, within the sediment were anoxic and pyrite precipitation took place within those deposits. The fact that pyrite in the black shale is not layered but disseminated in the rock agrees with this conclusion. We can then deduce that the initial sediment was free from authigenic pyrite and apatite. The

portion of the sediment column in which authigenic pyrite and apatite have not yet precipitated is defined as Zone 1.

4. Early diagenesis of the Toyoma Formation

Three diagenetic zones are thus defined. As sediments become buried deeper and deeper, they pass successively from Zone 1 to Zone 3.

(1) Zone 1

Zone 1 is the oxic portion of surface sediments; pelitic sediments rich in organic matter deposited in the continental shelf or in channel-slopes (Kamada, 1998). As described earlier, seawater in the sedimentary basin was not anoxic but oxic. Thus iron-manganese oxides or hydroxides were deposited and retained in the pelitic sediments.

The Zone 1 sediment is underlain by the anoxic sediment of Zone 2, in which microbial sulfate reduction proceeds. A fraction of hydrogen sulfide formed in the zone diffused upward to Zone 1 (Fig. 16). Because of this, sulfur-oxidizing bacteria grow in the Zone 1 sediments. Sulfuric acid was thus formed and pH of the interstitial water became lower than that of seawater (pH=8.2). This resulted in the dissolution of biogenic phosphate debris (fish bones, scales, teeth) contained in the sediment and the total phosphate concentrations of the interstitial water increased.

Since Zone 2 is anoxic, the lower part of Zone 1 must be suboxic, with a diminished concentration of molecular oxygen in the pore water. The reduction of iron-manganese oxides or hydroxides contained in the sediments proceeds in this portion liberating bivalent ions of iron and manganese to the interstitial water. These ions are the sources of pyrite and manganese-rich calcite which precipitate in the subsequent stages of diagenesis.

(2) Zone 2

As sediment burial progressed, sediments with pore water would have become anoxic. As a result, sulfur-oxidizing bacteria became extinct and sulfate-reducing bacteria, which are strictly anaerobic, began to grow. Hydrogen sulfide formed through sulfate reduction reacted with Fe^{2+} ion in the interstitial water leading to the precipitation of iron monoxide (FeS). The iron monoxide is finally transformed to pyrite (FeS_2) but the details of the process have not yet been understood. The isotopic sulfur composition of framboidal pyrite precipitated at this zone is about -50 to -40 ‰, judging from the results of SIMS analysis.

Which mineral of the two, pyrite or apatite, precipitates earlier within Zone 2, is not clear from the present data. However, the precipitation of apatite in Zone 2 is thought to be the result of the following conditions:

1. Owing to the dissolution of biogenic phosphate debris in Zone 1, the concentration of total phosphate ion ($\text{H}_3\text{PO}_4 + \text{H}_2\text{PO}_4^- + \text{HPO}_4^{2-} + \text{PO}_4^{3-}$) in the interstitial water increased.
2. The progress of sulfate reduction in Zone 2 increases the carbonate alkalinity and HCO_3^- concentration of the interstitial water. This will raise the pH value of the water causing an increase in the PO_4^{3-} fraction of the phosphate ions.

Therefore, we posit that the precipitation of apatite was due to the occurrence of sulfate reduction and that the precipitation of apatite succeeded that of iron sulfide (a precursor of pyrite).

Apatite precipitates whereas calcite does not in Zone 2. This may be ascribed to the difference in the solubility product constants for the minerals. Since the solubility product constant of calcite is much larger than that of fluorapatite (calcite $K_{sp} = 10^{-8.35}$; fluorapatite $K_{sp} = 10^{-60.4}$; Krauskopf, 1979), the pore water did not become super-saturated with calcite in Zone 2.

(3) Zone 3

This zone is defined by the onset of calcite precipitation. As the burial of the sediment progressed, sulfate reduction proceeded. Because of the decrease in SO_4^{2-} in pore water, carbonate alkalinity increased further. Consequently, calcite began to precipitate. The calcite is rich in Mn^{2+} , whose origin is inferred to be not clastic silicate minerals but manganese oxide or hydroxides precipitated from oxic seawater.

Zone 3 has been defined as the zone where only calcite precipitates. The C-type rock has X_{Pyrite} and X_{Apatite} values close to 0. Thus it is obvious that the interstitial water was depleted in pyrite and apatite components when the veins of C-type rock formed. However, the possibility that small amounts of pyrite or apatite co-precipitated with calcite at the beginning of Zone 3 is not precluded. The exact depth in which pyrite and apatite ceased to precipitate is not determinable from the present data.

5. Formative process of each rock type

The zone where each mineral precipitates is shown in Fig. 18.

(1) Phosphatic nodules

The initial sediments underwent the dissolution of biogenic phosphate debris in Zone 1. As time passed, the sediments reached the burial depth for Zone 2 and sulfate reduction began to take place. As a result, framboidal pyrite of $\delta^{34}\text{S} = -50$ to -40% precipitated in the sediments in a dispersed fashion (Fig. 19(a)). We surmise that soon after the onset of pyrite precipitation, apatite started to crystallize with some pre-existing seeds as nuclei to form porous phosphatic nodule precursors (Fig. 19(b)). We

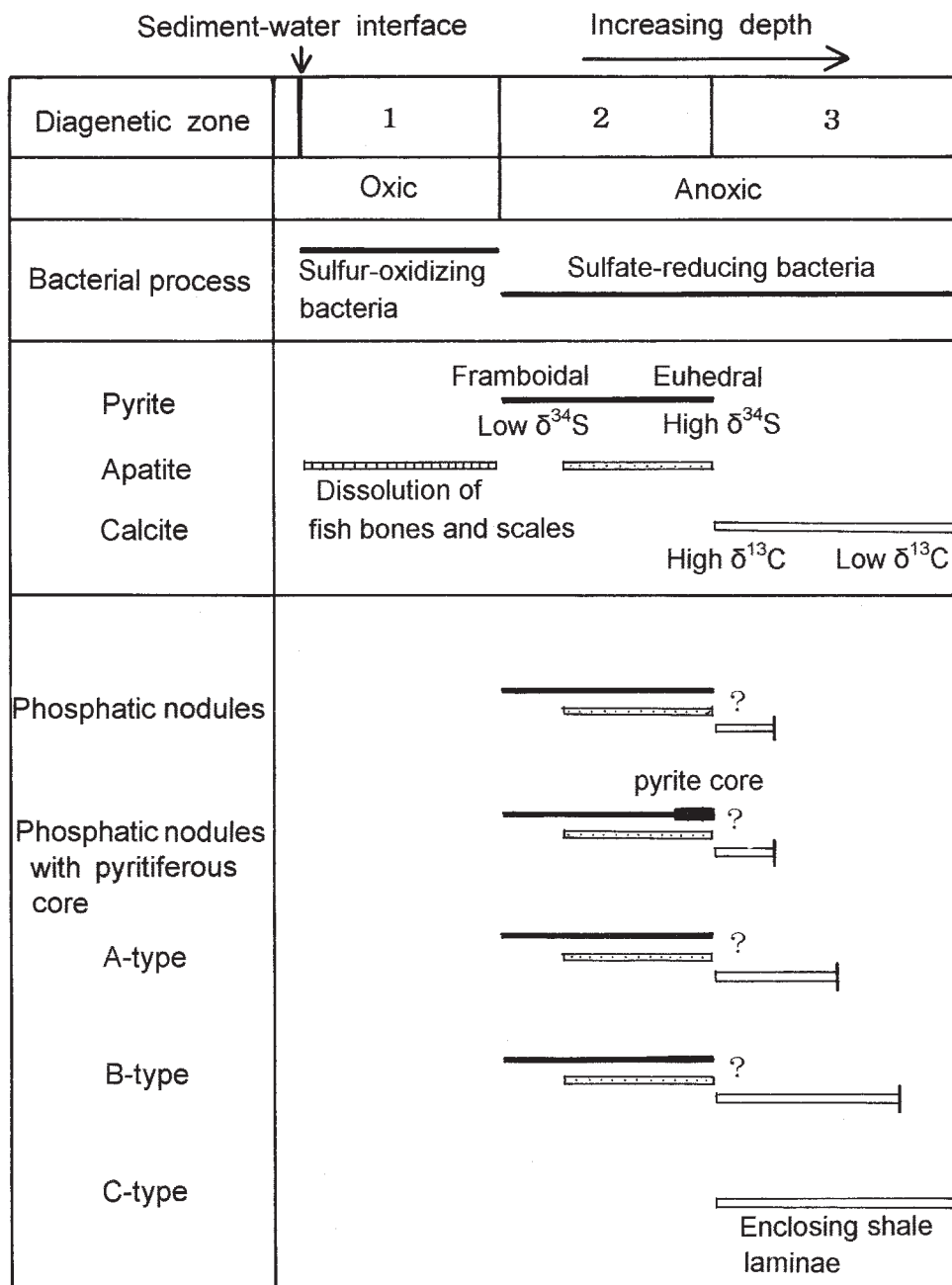


Fig. 18. Diagenetic zones and ranges of authigenic mineral precipitation with progressive burial in the Toyoma Formation.

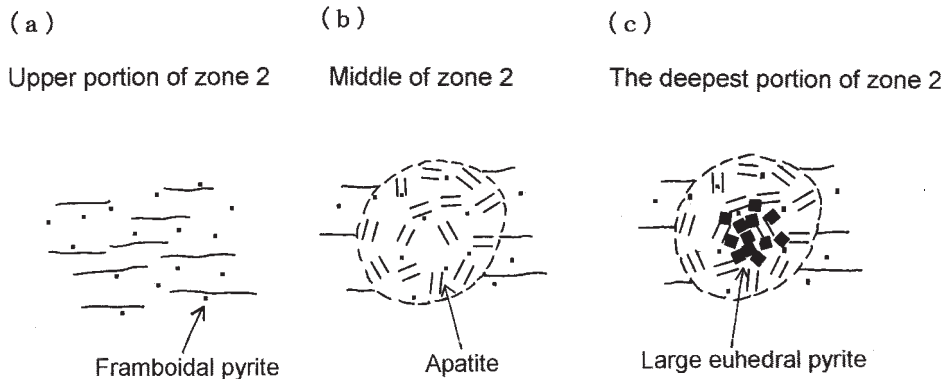


Fig. 19. Development of phosphatic nodules with pyritiferous cores. (a) Upper portion of Zone 2. Framboidal pyrite precipitates in a dispersed fashion. (b) Middle of Zone 2. Apatite precipitates to form a compaction-resistant framework. (c) Deep in Zone 2. Large euhedral pyrite precipitates in the inner part of the nodule.

infer that precipitation of apatite in the nodules formed a compaction-resistant framework. This allowed interstices filled with pore water to survive until the sediment reached the deeper part of Zone 2. At that point, large euhedral pyrite of high $\delta^{34}\text{S}$ precipitated in the center of the nodules from the evolved interstitial water (Fig. 19(c)). This produced the subtype of phosphatic nodules designated as *phosphatic nodules with pyritiferous cores*. The period of euhedral pyrite precipitation at the core is deduced to occur not in Zone 3 but at the end of Zone 2, owing to the fact that the pyrite is not accompanied by calcite.

Most of the phosphatic nodules continued to grow until the sediment reached Zone 3. As a result, calcite precipitated inside the nodules and the nodules became calcareous. Even after the inner parts of the nodules had consolidated, carbonate-rich fluid continued to segregate from the surrounding pelitic sediments producing the carbonate-rich nodule rims (Plate I -2).

The $\delta^{13}\text{C}$ of the calcareous phosphatic nodules is the highest in all of the rocks of the Toyoma Formation. This indicates that the nodules were formed and consolidated at the shallowest position of all the rocks (Fig. 18).

(2) A-type rock

A-type rock occurs as thin calcareous mudstone beds rich in phosphate (Kanisawa and Ehiro, 1986). On the whole, A-type rock is richer in CO_2 than phosphatic nodules, and its calcite $\delta^{13}\text{C}$ tends to be lower than that in the phosphatic nodules (Fig. 5). However, the composition of A-type rock varies widely.

A-type rock possessing high P_2O_5 content has chemical-isotopic features similar to the phosphatic nodules, and the REE distribution pattern of A-type rock is the same

as the phosphatic nodules. From these similarities, it is obvious that A-type rock was formed through similar chemical processes as the phosphatic nodules, although the modes of their occurrence are different. We speculate that if seeds for the growth of apatite are present within sediments, phosphatic nodules are formed, otherwise an A-type rock bed is formed. The reason A-type rock occurs as thin layers may be explained as follows: With the increased sediment burial, the concentration of PO_4^{3-} of interstitial water exceeds the solubility product constant of apatite at some depth. At that point the apatite precipitates all at once at the same level of the sediment column forming an A-type rock bed.

The X_{shale} of A-type rock varies from 0.8 to 0.2. This value is smaller than the X_{shale} of the phosphatic nodules (0.8 to 0.5). This is because A-type rock contains much more calcite than the phosphatic nodules. This means that precipitation of calcite in the A-type rock continued at much deeper levels than in the phosphatic nodules (Fig. 18).

A-type beds often show a C-A-C sandwich structure as shown in Figs. 2-2 and 2-4. The $\delta^{13}\text{C}$ of the C-type rock lying on both sides of the A-type bed is lower than that of the central A-type rock. This phenomenon can be explained by the concept that the interstitial water, saturated with CaCO_3 components, permeated the A-type precursor, crystallizing calcite inside. This raised X_{calcite} of the A-type rock and decreased the $\delta^{13}\text{C}$. In the middle of Zone 3, A-type beds became completely consolidated. However, segregation of carbonate-rich aqueous water from surrounding sediments continued precipitating calcite on both sides of the A-type bed (Fig. 20(e)). Thus interbedded C-, A-, and C-type rocks were formed with different $\delta^{13}\text{C}$ values.

(3) B-type rock

B-type rock's source is sandstone. The B-type rock has a $\delta^{13}\text{C}$ slightly lower than the A-type rock, and slightly higher than the C-type rock. Therefore, calcite precipitation in B-type rock continued at depths deeper than that of the final consolidation of A-type rock. The whole-rock pyrite $\delta^{34}\text{S}$ of B-type rock is higher than that of A-type rock, although the isotopic variation is large ($\delta^{34}\text{S} = -19.3$ to -4.6%).

Some of the B-type rocks (sample 110A, U-B01, KT104, and U-SS04) have similar sulfur isotopic ratios and morphologies to the pyrite in the pyritiferous core of the phosphatic nodules. That is to say, large euhedral pyrite is dominant and the whole-rock pyrite $\delta^{34}\text{S}$ value is exceedingly high ($\delta^{34}\text{S} = -9.9$ to -4.6%). We infer that these pyrites were precipitated from the interstitial water at the deepest portion of Zone 2, in which $\delta^{34}\text{S}$ of sulfate ion was elevated.

The fact that whole-rock pyrite $\delta^{34}\text{S}$ of B-type rock is higher than that for A-type rock means that the proportion of high $\delta^{34}\text{S}$ -pyrite grains is higher in B-type than in

A-type rock. The dominance of high- $\delta^{34}\text{S}$ pyrite grains in B-type rock may be ascribed to the fact that the original rock is sandstone. The interstices in the B-type rock must have been preserved to a deeper part of Zone 2 against sediment compaction by support of its clastic mineral grains. This also explains why calcite continued to precipitate until the middle of Zone 3 in B-type rock.

(4) C-type rock

The $\delta^{13}\text{C}$ of CO_3^{2-} ions in the interstitial water dropped to -16% deep in Zone 3 owing to progressive oxidation of organic matter. The interstitial water, saturated in CaCO_3 components, segregated from the pelitic sediments, probably due to the progress of compaction. Thus, a segregation layer consisting of calcite and an enclosing thin film of black shale was formed (Fig. 2-2, -3). This is the C-type carbonate rock. Some of the carbonate-supersaturated solution intruded into the black shale, forming carbonate veins (Fig. 2-5), at which time the black shale was fragmented and its fragments were enclosed in C-type rock (Plate I-5). The fragmentation of black shale needs a pressure release, which might be caused by the decomposition of CO_2 -hydrate which had once formed within the sediments.

(5) Black shale

The black shale contains neither apatite nor calcite. It carries only pyrite as an authigenic mineral and that pyrite is exclusively framboidal and minute-type grains. However, sulfate reduction must have proceeded within the organic-rich pelitic sediments that were the parent material of the black shale. This indicates that the products of sulfate reduction, such as phosphate and carbonate, were removed from the pelitic sediments in the form of a solute in aqueous solution.

The slaty cleavages develop well in the black shale but not in the phosphatic nodules nor A-, B-, and C-type rocks. The reason apatite, calcite and the pyrite precipitated at later-stages is not retained in the black shale is thought to be related to sediment compaction. The progress of compaction will squeeze phosphate- and carbonate-bearing aqueous solution from the sediments. The solution then migrates to that part of the sediments where interstices are preserved against sediment compaction, precipitating apatite, later-stage pyrite, and calcite.

6. Diagenetic segregation

The authigenic minerals occurring in sedimentary rock are thought to fill interstices possessed by the original rock. Let us consider a model phosphatic nodule which has the composition of $X_{\text{Shale}}=0.7$, $X_{\text{Pyrite}}=0.15$ and $X_{\text{Apatite}}=0.15$ mole fractions. It is supposed that pyrite and apatite filled the interstices of the original sediments. The porosity (volume of interstices/total volume) is calculated to be 0.64 for this rock. The

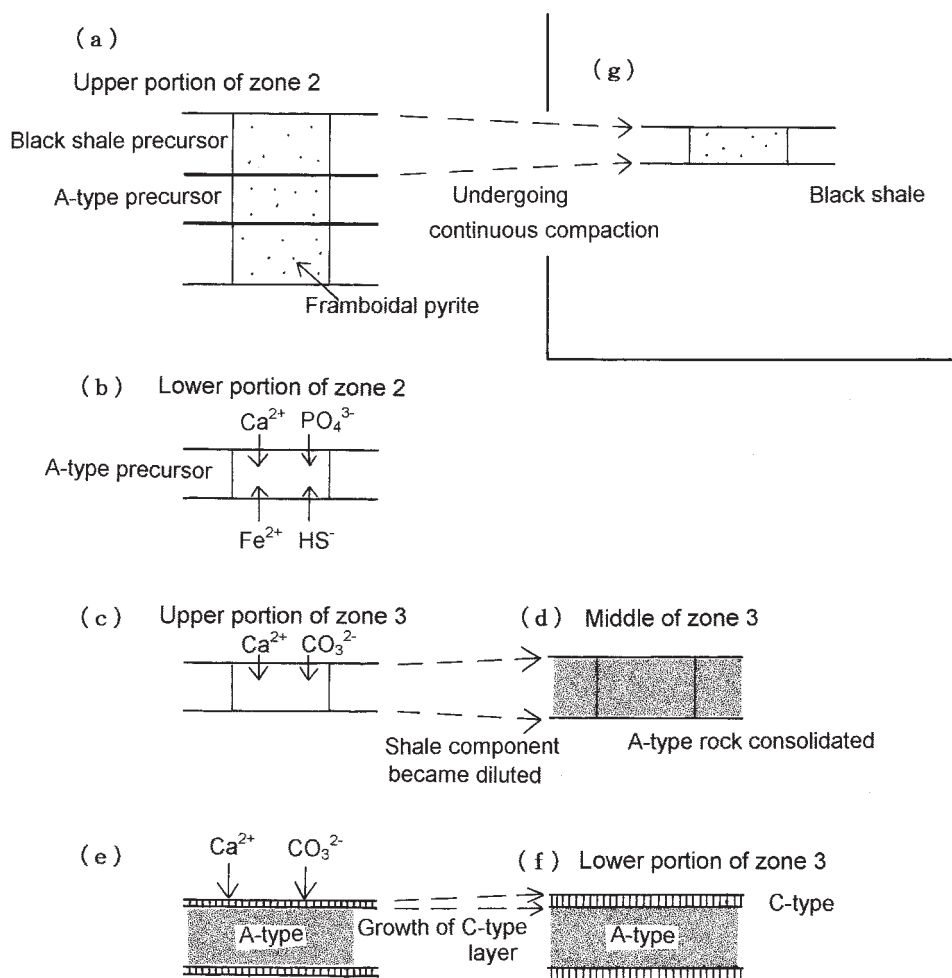


Fig. 20. Development of A- and C-type rock segregation layers. (a) Pyrite precipitates within A-type rock precursor (i.e., black shale) in the upper portion of Zone 2. (b) Middle to lower Zone 2. Apatite, in addition to pyrite, precipitates within the A-type rock precursor. (c) Upper Zone 3. The A-type segregation layer grows as sulfate reduction in the surrounding pelitic sediments progresses. The amount of calcite precipitated is much larger than needed to fill interstitial pores in the black shale, resulting in the dilution of initial clastic material content in A-type rock. (d) Middle of Zone 3. The A-type layer finally becomes consolidated. But carbonate ion flux from the pelitic sediments continues. (e) C-type segregation layer grows on both sides of the A-type layer. (f) Lower Zone 3. C-type rock becomes consolidated. (g) Black shale at present.

value is close to the estimated porosity value of clastic rocks of continent origin (Einsele, 1992). Thus it is safe to assume that authigenic minerals fill the interstices of the initial sediments, at least for the phosphatic nodules.

However, X_{Shale} values for A- and C-type rock decrease clearly with decreasing $\delta^{13}\text{C}$, as shown in Fig. 12. This means that the sum of the X values for authigenic minerals (i.e., $X_{\text{Pyrite}} + X_{\text{Apatite}} + X_{\text{Calcite}}$) increases with decreasing $\delta^{13}\text{C}$. When we calculate the porosity of one A-type rock (UP-11, $\delta^{13}\text{C} = -10.5\text{‰}$, $X_{\text{Shale}} = 0.23$) under the assumption that the total volume of authigenic minerals is equal to the volume of interstices possessed by the original sediment, the porosity is calculated to be 0.89. Clearly the porosity value increased with the decrease of $\delta^{13}\text{C}$. Since porosity decreases with the progress of sediment burial (Einsele, 1992), the tendency seen in Fig. 12 does not coincide with the view that the total volume of authigenic minerals in a rock represents the volume of interstices the rock contained.

The A- and C-type rocks, having lower X_{Shale} than the phosphatic nodules, were formed through the following process: The amount of authigenic minerals precipitated was much larger than needed to fill interstitial pores in pelitic sediments, which resulted in the "dilution" of initial clastic material content. With such a process, segregation layers or veins would develop. The formative process for A- and C-type rock through segregation is shown in Fig. 20. This scenario can successfully explain the origin of the observed C-A-C sandwich structure and the difference in $\delta^{13}\text{C}$ values between interbedded A- and C-type beds. Thus, we conclude that diagenetic phosphatic and carbonate rocks in the Toyoma Formation were not formed simply by cementing the interstitial pores of the sediments, but were formed through the growth of a segregation layer composed of authigenic minerals.

VII Conclusions

We reached the following conclusions in the present study.

1. Phosphatic and carbonate rocks of the Toyoma Formation in Northeastern Japan were formed by microbial sulfate reduction during the early diagenesis of organic-rich sediments. The authigenic minerals precipitated from pore water are pyrite, apatite, and calcite.

2. The $\delta^{34}\text{S}$ of individual pyrite grains in a phosphatic nodule was analyzed by using a high-resolution secondary ion mass spectrometer. Intergranular differences in the $\delta^{34}\text{S}$ of a rock sample as large as 37‰ were measured. Diagenetic phosphatic and carbonate rocks in the Toyoma Formation are a mixture of authigenic minerals of differing-stage origins, except for some C-type rocks.

3. In spite of this mixed condition, it was possible to determine the stage of diagenesis in which each rock type was formed by considering the $\delta^{13}\text{C}$ of the calcite, the variation of mole fractions of authigenic minerals, the total-rock pyrite $\delta^{34}\text{S}$ and

the modal proportion of pyrite types. The early diagenesis of the Toyoma Formation has been divided into three diagenetic zones; 1, 2, and 3. Zone 1 is the region of initial sediment distribution and is oxic. Zone 2 is an anoxic zone in which microbial sulfate reduction took place. Zone 3 is the zone of calcite precipitation. Sediments passed through each successive zone owing to increased sediment burial.

4. The source of phosphorus for the phosphatic rocks is deduced to be biogenic phosphate debris such as fish bones, scales and teeth, according to their Y, La, and Ce contents.

5. Sulfur-oxidizing bacteria grew in the Zone 1 sediments and produced sulfuric acid, which dissolved biogenic phosphate debris. As burial of the sediment progressed, the former oxic surface layer became anoxic, initiating sulfate reduction, which led to the precipitation of apatite.

6. The phosphatic and carbonate rocks of the Toyoma Formation were formed by segregation layer growth during diagenesis. Although the segregation of carbonate ions from the sediments continued until the later stages of sulfate reduction, the segregation layers became successively closed with respect to ion flux. As a result, interbedded A-, B-, and C-type rocks were formed with different $\delta^{13}\text{C}$ values.

Acknowledgements

Sulfur isotopic analysis was conducted at the Institute of Geology, the Graduate School of the University of Tokyo. The authors wish to thank Prof. H. Shimazaki for providing access to the laboratory. In the early stage of this work, experiments on sulfur isotopes were done at the Department of Earth Science, Nagoya University. The authors also wish to thank the late Prof. N. Nakai of the Department. The authors wish to express their gratitude to Prof. M. Ehiro of Tohoku University and Prof. R. Matsumoto of the University of Tokyo for helpful discussions. The authors are also grateful to Prof. Y. Miyake and Dr. K. Yoshida of Shinshu University for a critical reading of the manuscript.

Postscript

The Sanriku coast, including the study area, was hit by the enormous tsunami caused by the Great East Japan Earthquake on the 11th of March, 2011. Approximately twenty thousand lives were lost and the coastal towns were completely destroyed. The authors extend their heartfelt condolences to the victims of the earthquake and tsunami disaster.

References

- Berner, R. A., 1971, *Principles of chemical sedimentology*. McGraw-Hill, New York, 240p.
Canfield, D. E., 2001, Biogeochemistry of sulfur isotopes. *In* Stable isotope geochemistry, Rev.

- mineral. geochem., **43**, 607-636.
- Claypool, G. E., Holser, W. H., Kaplan, I. R., Sakai, H. and Zak, I., 1980, The age curves of sulfur and oxygen isotopes in marine sulfate and their mutual interpretation. *Chem. Geol.*, **28**, 199-260.
- Ehiro, M. and Bando, Y., 1985, Late Permian ammonoids from the Southern Kitakami Massif, Northeast Japan. *Trans. Proc. Palaeontol. Soc. Japan*, **137**, 25-49.
- Einsele, G., 1992, *Sedimentary Basins, Evolution, Facies and Sediment Budget*. Springer-Verlag, 628p.
- Elderfield, H. and Pagett, R., 1986, Rare earth elements in ichthyoliths: Variation with redox conditions and depositional environment. *Science Total Environ.*, **49**, 175-197.
- Endo, Y., Katada, M. and Sasaki, A., 1973, Pyrite in the Permian Toyoma Formation of the Southern Kitakami Mountains, Japan. *Bull. Geol. Sur. Jpn.*, **24**, 113-121.*
- Gulbrandsen, R. A., 1970, Relation of carbon dioxide content of apatite of the Phosphoria Formation to regional facies. *U.S. Geol. Surv. Prof. Pap.*, **700-B**, 9-13.
- Hennessy, J. and Knauth, L. P., 1985, Isotopic variations in dolomite concretions from the Monterey formation, California. *Jour. Sed. Petr.*, **55**, 120-130.
- Hoefs, J., 1987, *Stable isotope geochemistry, third edition*. Springer-Verlag, New York, Heidelberg, Berlin, 241p.
- Irwin, H., Curtis, C. and Coleman, M., 1977, Isotopic evidence for source of diagenetic carbonates formed during burial of organic-rich sediments. *Nature*, **269**, 209-213.
- Kamada, K., 1993, *Geology of the Tsuya District. With Geological Sheet Map at 1 : 50,000*. Geol. Surv. Jpn., 70p.*
- Kamada, K., 1998, Upper Permian channel-slope deposits of the Toyoma Formation in the Tsuya area in the Southern Kitakami Belt, Northeast Japan. *Earth Sci.*, **52**, 453-463.
- Kampschulte, A. and Strauss, H., 2004, The sulfur isotopic evolution of Phanerozoic seawater based on the analysis of structurally substituted sulfate in carbonates. *Chem. Geol.*, **204**, 255-286.
- Kanaya, H. and Katada, M., 1975, Contents of Thorium, Uranium and Potassium of the upper Permian mudstones and sandstones in the Southern Kitakami Mountains, Japan. *Jour. Japan. Assoc. Min. Petr. Econ. Geol.*, **70**, 286-294.
- Kanisawa, S., Ehiro, M., Yoshida, T., and Aoki, K., 1985, Geochemical characteristics of phosphatic rocks and carbonate rocks in the shales from the Permian Toyoman Series, Kitakami Mountains. *Res. Rep. Lab. Nuclear Sci., Tohoku Univ.*, **18**, 403-413.**
- Kanisawa, S. and Ehiro, M., 1986, Occurrence and geochemical nature of phosphatic rocks and Mn-rich carbonate rocks in the Toyoman Series, Kitakami Mountains, Northeastern Japan. *Jour. Japan. Assoc. Min. Petr. Econ. Geol.*, **81**, 12-31.
- Kolodny, Y., 1981, Phosphorites. In Emiliani, C. ed., *The Sea, ideas and observations on progress in the study of the seas*, Wiley Interscience, New York, **7**, 981-1023.
- Krauskopf, K. B., 1979, *Introduction to Geochemistry, 2nd ed.*. McGraw-Hill, New York, 617p.
- Longstaffe, F. J., 1989, Stable isotopes as tracers in clastic diagenesis. In Hutcheon, I. E. ed., *MAC Short course in burial diagenesis*, **15**, 201-277.
- McCrea, J. M., 1950, The isotopic chemistry of carbonates and a paleotemperature scale. *Jour.*

- Chem. Phys.*, **18**, 849-857.
- Minato, M., 1950, Toyoma-Sea, the Late Permian Inland-Sea in the Kitakami Mountainland, Honshu, Japan. *Proc. Jpn. Acad.*, **26**, 80-86.
- Morikiyo, T., Iwamasa, K., Kanisawa, S. and Ehiro, M., 1994, Origin of the phosphate and carbonate rocks in the Toyoman Series, Kitakami Mountains, northern Japan-Carbon and sulfur isotopic study. *Earth Sci.*, **48**, 417-431.*
- Morikiyo, T. and Matsunaga, K., 2000, Oxygen isotopic alteration of carbonates in the non-metamorphosed calcareous shale and sandstone from the South Kitakami Belt, northeastern Japan. *Earth Sci.*, **54**, 153-158.*
- Morikiyo, T. and Matsunaga, K., 2001, Origin of phosphatic rocks and carbonate rocks in the Toyoma Formation, Northeastern Japan. *Extended abstr. 11th Annual Goldschmidt Conf.*, # 3066.
- Morikiyo, T., Matsunaga, K., Iwamasa, K., and Kanisawa, S., 2004, The source of phosphorus for the phosphatic rocks in the Toyoma Formation. *Jour. Fac. Sci. Shinshu Univ.*, **39**, 19-24.
- Morishita, Y., Sasaki, A., Kita, N. T. and Togashi, S., 1997, Microanalysis for sulfur and oxygen isotopic ratios using SIMS. In Gillen, G., Lareau, R., Bennett, J and Stevie, F. eds., Secondary Ion Mass Spectrometry SIMS XI, 67-70.
- Nathan, Y. and Nielsen, H., 1980, Sulfur isotopes in phosphorites. In Bendor, Y. K. and Scripps Institution of Oceanography eds., Marine phosphorites-Geochemistry, Occurrence, Genesis, SEPM Spec. Pub., **29**, 73-78.
- Nielsen, H., 1978, Sulfur isotopes in nature, In Wedepohl, K. H. ed., Handbook of Geochemistry. Springer-Verlag, Chapter 16-B, B1-B40.
- Pettijohn, E. J., 1975, *Sedimentary rocks*, 3rd ed. Harper & Row, New York, 628p.
- Sharma, T. and Clayton, R. N., 1965, Measurement of O¹⁸/O¹⁶ ratios of total oxygen of carbonates. *Geochim. Cosmochim. Acta*, **29**, 1347-1354.
- Shimazaki, H., 1985, Regional variation of isotopic composition of hydrothermal ore sulfur in Japan. *Jour. Fac. Sci. Univ. Tokyo, Sec. 2*, **22**, 81-100.
- Strauss, H., 1997, The isotopic composition of sedimentary sulfur through time. *Palaeogeogr. Palaeoclimat. Palaeoecol.*, **132**, 97-118.
- Terashima, S., Ando, A., Okai, T., Kanai, Y., Taniguchi, M., Takizawa, F., and Itoh, S., 1990, Elemental concentrations in nine new GSJ rock reference samples "Sedimentary rock series". *Geostand. Newslet.*, **14**, 1-5.
- Wignall, P. G., 1994, *Black shales*. Oxford monograph on Geology and Geophysics. **30**, 127p.
- Yamanaka, T., Aso, I., Togashi, S., Tanigawa, M., Shoji, K., Watanabe, T., Watanabe, N., Maki, K. and Suzuki, H., 2002, Corrosion by bacteria of concrete in sewerage systems and inhibitory effects of formates on their growth. *Water Res.*, **36**, 2636-2642.
- Yanagisawa, F. and Sakai, H., 1983, Thermal decomposition of barium sulfate-vanadium pentaoxide-silica glass mixtures for preparation of sulfur dioxide on sulfur isotope ratio measurements. *Anal. Chem.*, **55**, 985-987.

* : in Japanese with English abstract

** : in Japanese

Appendix

Procedure for calculating mole fractions of shale (X_{Shale}), pyrite (X_{Pyrite}), apatite (X_{Apatite}), and calcite (X_{Calcite}) from whole-rock chemical composition.

A. In cases where the complete chemical analyses are available (Table 4-1).

$$X_{\text{Shale}} = \text{SiO}_2 \text{ wt.}\% / 59.31$$

(59.31 : average value of SiO_2 content for samples JSL-1 and JSL-2)

$$X_{\text{Apatite}} = \text{P}_2\text{O}_5 \text{ wt.}\% / 42.22$$

(42.22 : P_2O_5 content of ideal fluorapatite, $\text{Ca}_5(\text{PO}_4)_3\text{F}$)

$$X_{\text{Calcite}} = \text{CO}_2 \text{ wt.}\% / 43.84$$

(43.84 : CO_2 content of the following calcite $\text{Ca}_{0.94}\text{Mg}_{0.02}\text{Fe}_{0.01}\text{Mn}_{0.03}\text{CO}_3$)

$$\text{FeO}^*(\text{total iron as FeO}) - (\text{FeO}^* \text{ in shale} + \text{FeO} \text{ in calcite}) = \text{FeO} \text{ from pyrite}$$

$$\text{FeO}^* \text{ in shale}(\%) = 6.06X_{\text{Shale}}, \text{FeO} \text{ in calcite}(\%) = 0.72X_{\text{Calcite}}$$

$$X_{\text{Pyrite}} = \text{FeO} \text{ wt.}\% \text{ from pyrite} / 59.86$$

(59.86 : FeO content of ideal pyrite, FeS_2)

B. In cases where only partial analyses are available (Tables 4-2).

From Table 4-1, it can be seen that the sum of X values is always close to 1. Thus, the assumption that X values total to 1.0 is adopted.

$$X_{\text{Apatite}} = \text{P}_2\text{O}_5 \text{ wt.}\% / 42.22$$

$$X_{\text{Calcite}} = \text{CO}_2 \text{ wt.}\% / 43.84$$

$$X_{\text{Shale}} + X_{\text{Pyrite}} + X_{\text{Apatite}} + X_{\text{Calcite}} = 1$$

$$6.06X_{\text{Shale}} + 59.86X_{\text{Pyrite}} + 0.72X_{\text{Calcite}} = \text{FeO}^* \text{ wt.}\%$$

X_{Shale} and X_{Pyrite} values can be obtained by solving the simultaneous equations above.

C. Calculations involving B-type rock (Table 4-2).

For the calculation of B-type rock, the chemical composition of average graywacke ($\text{FeO}^* = 4.9\%$, Pettijohn, 1975) is used. Thus,

$$X_{\text{Apatite}} = \text{P}_2\text{O}_5 \text{ wt.}\% / 42.22$$

$$X_{\text{Calcite}} = \text{CO}_2 \text{ wt.}\% / 43.84$$

$$X_{\text{Sandstone}} + X_{\text{Pyrite}} + X_{\text{Apatite}} + X_{\text{Calcite}} = 1$$

$$4.9X_{\text{Sandstone}} + 59.86X_{\text{Pyrite}} + 0.72X_{\text{Calcite}} = \text{FeO}^* \text{ wt.}\%$$

$X_{\text{Sandstone}}$ and X_{Pyrite} values are obtained by solving the simultaneous equations above.

PLATES AND EXPLANATIONS

(with 4 Plates)

Plate I

- 1 Phosphatic nodule (no pyritiferous core subtype) in black shale. The internal parts of the nodule are not homogeneous but zoned.
- 2 Phosphatic nodule (no pyritiferous core subtype) in black shale occurring at the seaside. The marginal part of the nodule has been corroded indicating that the part was rich in carbonate mineral.
- 3 Phosphatic nodule with a pyritiferous core.
- 4 A hand specimen of interbedded A-, B- and C-type rocks. The A-type rock layer shows a C-A-C sandwich structure and so does the B type rock layer.
- 5 The thick portion of C-type bed. Abundant rectangular fragments of black shale several centimeters in size are enclosed in the C-type bed.
- 6 Thin wavy films of black shale (arrow) in C-type rock. The structure must be formed through the *lit-par-lit* injection of carbonate-rich aqueous solution into black shale.

Plate I

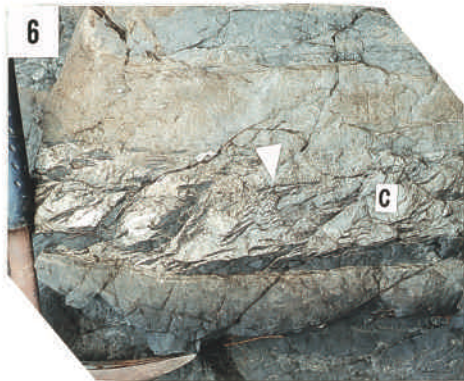
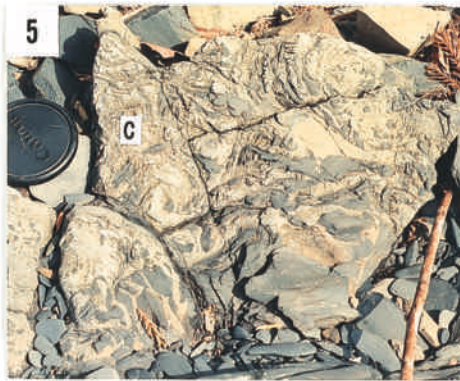
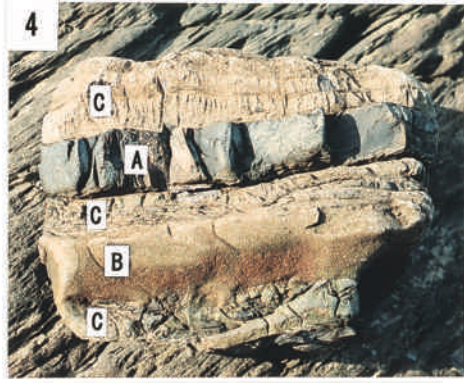


Plate II

Photomicrographs of various rocks from the Toyoma Formation. The scales are 0.1 mm long in all figures.

- 1 Framboidal pyrite in black shale. Pressure shadows fulfilled with chlorite are clearly seen. Open nicol. (Sp. KI03-2)
- 2 Framboidal pyrite accompanied by ring-shaped aggregates of minute pyrite. Open nicol. (Sp. KI03-2)
- 3 and 4 Spheluritic fossil-like material in a phosphatic nodule. It is probably the remain of radiolarians. 3 : open nicol, 4 : crossed nicols. (Sp. U-N171)
- 5 Small-sized euhedral pyrite forming a circular structure in a phosphatic nodule. Open nicol. (Sp. KI01-4)
- 6 Zoned calcite in B-type calcareous sandstone. The core of the calcite crystal is brownish in color while the margin is colorless and transparent. Open nicol. (Sp. KI02-3b)

Plate II

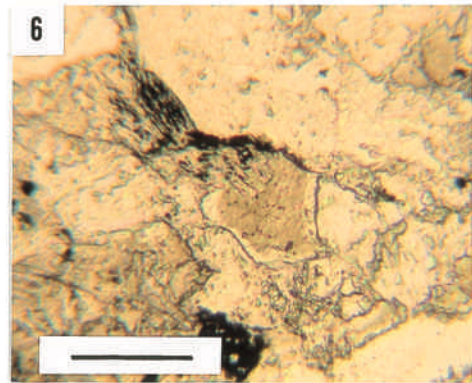
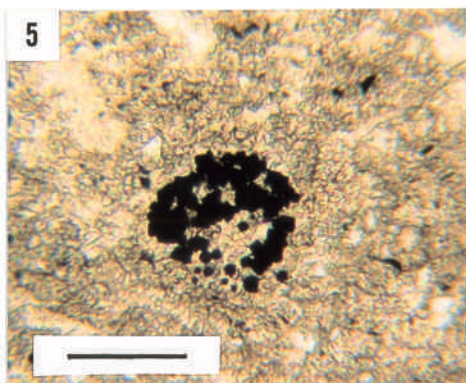
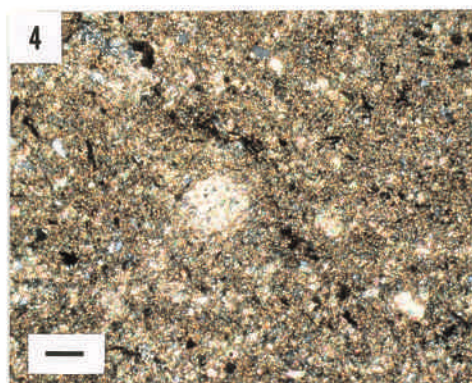
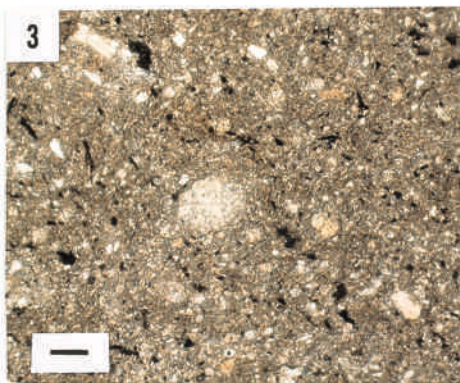
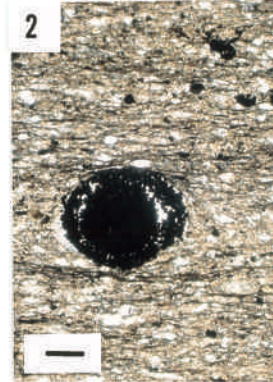
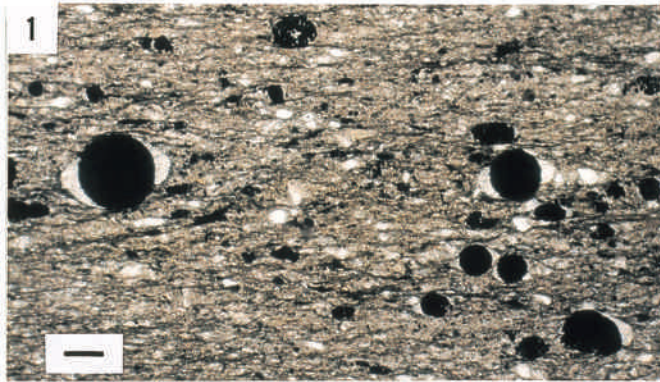


Plate III

Photomicrographs of various rocks from the Toyoma Formation. The scales are 0.1 mm long in all figures.

- 1 and 2 A-type rock (phosphate-bearing calcareous mudstone). Pyrite spherules (framboidal pyrite) and lens-shaped clusters of small-sized pyrite crystals are present. 1 : open nicol, 2 : crossed nicols. (Sp. U-A07)
- 3 and 4 B-type rock (calcareous sandstone). Pyrite in B-type rock is mostly large and euhedral, and framboidal pyrite is scarce. The cement is calcite as displayed by high interference color in 4. 3 : open nicol, 4 : crossed nicols. (Sp. U-B04)
- 5 and 6 C-type rock (carbonate rock). The dark, thin wavy bands (as indicated by array) are thin films of black shale enclosed in the C-type rock. C-type rock is composed of bladed crystals of sparry calcite which show parallel alignment. 5 : open nicol, 6 crossed nicols. (Sp. 89042902sp3c)

Plate III

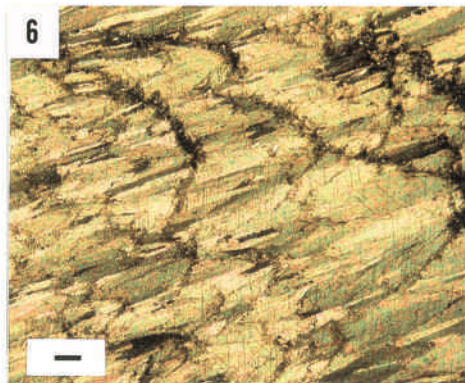
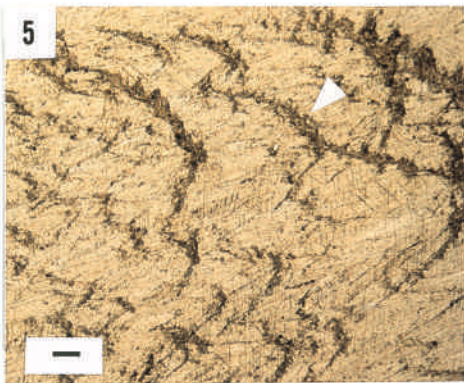
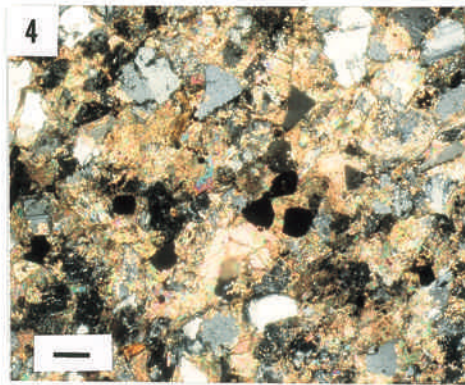
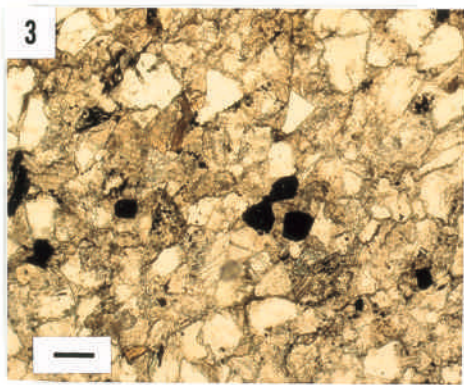
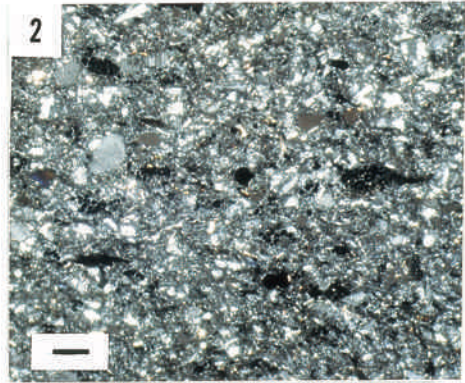
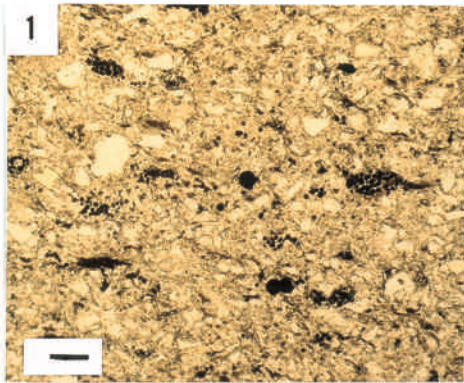


Plate IV

Back scattered electron images (COMPO images) of pyrite. Accelerating voltage is 25 kV and the scales are 10 μm long in all figures.

- 1 Spherical aggregate of euhedral, minute crystals of pyrite (framboidal pyrite) accompanied by the cluster of euhedral, minute pyrite crystals in black shale. (Sp. U-SH01)
- 2 Higher magnification ($\times 2000$) of the sample shown in the preceding figure. Pyrite crystals are all euhedral.
- 3 Framboidal pyrite accompanied by the nebulitic aggregate of minute pyrite crystals. (Sp. U-SH01, black shale)
- 4 A large number of framboidal pyrite occurring in the nebulitic cluster of minute pyrite crystals. (Sp. U-SH01, black shale)
- 5 Subhedral crystals of pyrite possessing small spaces inside. This may indicate that large euhedral pyrite crystals are formed through grain coalescence of minute or framboidal pyrite. (Sp. U-B01, B-type rock)
- 6 Large euhedral pyrite. (Sp. U-C09, C-type rock)

Plate IV

